Charge Density Wave in the New Polymorphs of $RE_2Ru_3Ge_5$ (*RE* = Pr, Sm, Dy)

Daniel E. Bugaris,[†] Fei Han,[†] Christos D. Malliakas,[‡] Nicholas P. Calta,[‡] Mihai Sturza,[†,◊] Matthew Krogstad,[†,Δ] Raymond Osborn,[†] Stephan Rosenkranz,[†] Jacob P.C. Ruff,[∂] Giancarlo Trimarchi,[‖] Sergey L. Bud'ko,[§] Mahalingam Balasubramanian,[⊥] Duck Young Chung,[†] Mercouri G. Kanatzidis[*,†,‡]

[†] *Materials Science Division, Argonne National Laboratory, Argonne, IL 60439, USA*

[‡] *Department of Chemistry, Northwestern University, Evanston, IL 60208, USA*

[◊] *Leibniz Institute for Solid State and Materials Research Dresden IFW, Institute for Solid State Research, 01069 Dresden, Germany*

[Δ] *Department of Physics, Northern Illinois University, DeKalb, IL 60115, USA*

[∂] *Cornell High Energy Synchrotron Source, Cornell University, Ithaca, NY 14853, USA*

[‖] *Department of Physics and Astronomy, Northwestern University, Evanston, IL 60208, USA*

[§] *Division of Materials Science & Engineering, Ames Laboratory, and Department of Physics and Astronomy, Iowa State University, Ames, IA 50011, USA*

[⊥] *X-ray Science Division, Argonne National Laboratory, Argonne, IL 60439, USA*

ABSTRACT: A new polymorph of the $RE_2Ru_3Ge_5$ (*RE* = Pr, Sm, Dy) compounds has been grown as single crystals via an indium flux. These compounds crystallize in tetragonal space group *P*4/*mnc* with the $Sc_2Fe_3Si_5$-type structure, having lattice parameters a = 11.020(2) Å and c = 5.853(1) Å for *RE* = Pr, a = 10.982(2) Å and c = 5.777(1) Å for *RE* = Sm, and a = 10.927(2) Å and c = 5.697(1) Å for *RE* = Dy. These materials exhibit a structural transition at low temperature that occurs due to the charge density wave (CDW). Both the high-temperature average crystal structure and the low-temperature incommensurately modulated crystal structure (for $Sm_2Ru_3Ge_5$ as a representative) have been solved. The charge density wave order arises due to periodic distortions of the one-dimensional zig-zag Ge chains. From X-ray diffraction, charge transport (electrical resistivity, Hall effect, magnetoresistance), magnetic measurements, and heat capacity, the ordering temperatures (T_{CDW}) observed in the Pr and Sm analogues are ~ 200 K and ~ 175 K, respectively. The charge transport measurement results indicate an electronic state transition happening simultaneously with the CDW transition. X-ray absorption near-edge spectroscopy (XANES) and electronic band structure results are also reported.

INTRODUCTION

The interactions between lattice distortions and electrons (charge or spin) may induce charge density waves (CDWs) or spin density waves (SDWs), among other phenomena, in a given material. CDWs arise from the coupling of electrons and phonons, resulting in periodic areas of low or high electron density, which can be commensurate or incommensurate with the crystallographic lattice periodicity. The symmetry breaking associated with this coupling happens at the phase transition temperature, T_{CDW}. Determining the exact crystal structure below T_{CDW} can be challenging due to the tiny amplitude of these effects, which produce only weak superlattice Bragg peaks that are difficult to resolve with X-rays, and then often can only be solved by advanced superspace crystallographic methodologies. Nevertheless, some combination of X-ray diffraction, transport property measurements, selected area electron diffraction (SAED), angle-resolved photoemission spectroscopy (ARPES), and/or scanning tunneling microscopy (STM) can be utilized to identify and characterize CDW materials with some confidence. SDWs are similar to CDWs in that they also develop from the spatial modulation of electron density; however, SDWs are attributed to electron spins rather than charge. In addition to the techniques mentioned above, SDW materials are typically distinguished by magnetic susceptibility and neutron diffraction measurements.

Density waves are most commonly manifest in metallic materials with anisotropic, low-dimensional structures such as 1D chains or 2D layers. Over the past decade, our group has investigated a variety of chalcogenides, pnictides, and intermetallics that exhibit CDWs or SDWs. For example, rare-earth polytellurides including *RE*Te_3 (*RE* = La-Nd, Sm, Gd-Tm), Sm_2Te_5, *AMRE*Te_4 (*A* = Na, K; *M* = Cu, Ag; *RE* = La, Ce), and $Cu_{0.63}EuTe_2$ display CDWs associated with 2D square nets of Te atoms.[1] Due to lattice distortions in these materials, the "infinite" Te square lattices devolve to various polytelluride oligomers with concomitant anomalies in the electronic transport behavior. We have also studied the canonical CDW material, 2*H*-$NbSe_2$, reporting the first detailed crystallographic structure below T_{CDW}.[2] In this compound, the density wave arises from the fluctuations in the Nb–Nb metal bond distances. *RE*$Co_{1-x}Ga_3Ge$ (*RE* = Gd, Y) were the first materials to be discovered with a CDW distortion in a square net of group 13 atoms (Ga).[3] Finally, $CaFe_4As_3$ was reported to exhibit spin density wave behavior with incommensurate and locked-in transitions at two different temperatures.[4]

CDWs and SDWs have received significant attention from the condensed matter chemistry and physics communities as these broken symmetry ground states are often observed in close proximity to superconductivity. For instance, spin density wave order in the parent compounds $BaFe_2As_2$[5] can be suppressed by hole-doping on the alkaline-earth site (with Na, K, etc…),[6] electron-doping on the Fe site (with Co, Ni, etc…),[7] isovalent substitution on the As site (with P),[8] or the application of external pressure.[9] The suppression of SDW order is followed by the appearance of superconductivity in this family of so-called 122 iron arsenides. This has motivated our search for novel materials with density wave behavior. As a result of this investigation, we have uncovered the family of CDW compounds $RE_2Ru_3Ge_5$ (*RE* = Pr, Sm, Dy). In the literature, these phases were previously reported to be synthesized by arc-melting, with the consequent structure refinements yielding $U_2Co_3Si_5$-type structures.[10] However, crystal growth using a molten indium flux yields a new polymorph of these materials with the $Sc_2Fe_3Si_5$-type structure. Through a combination of powder and single-crystal X-ray diffraction, charge transport measurements, magnetic measurements, and heat capacity, we thoroughly characterized the CDW state in these compounds. The results of X-ray absorption near-edge spectroscopy and electronic band structure calculations are also provided.

EXPERIMENTAL METHODS

General Details. The following reagents (in powder form) were used as received: praseodymium (Alfa Aesar, 99.9%), samarium (Alfa Aesar, 99.9%), dysprosium (Alfa Aesar, 99.9%), and ruthenium (Johnson Matthey, 99.999+%). Germanium lumps (Plasmaterials, 99.999%) were ground to a coarse powder prior to use. Indium shot (Plasmaterials, 99.999%) was briefly rinsed with dilute HCl to remove any surface oxide impurities. Initial manipulations were carried out in an M-Braun glovebox under an inert Ar atmosphere (< 0.1 ppm H_2O and O_2).

Crystal Growth of $RE_2Ru_3Ge_5$. The reaction mixtures consisted of rare-earth element (1.66 mmol), Ru 2.5 mmol), and Ge (4.16 mmol). The reagents were loaded into 2 mL alumina crucibles and covered with a large excess of In (~ 2 g) as flux. Next, the alumina crucibles were placed in 15 mm O.D. × 13 mm I.D. fused-silica tubes and flame-sealed under a vacuum of $< 10^{-4}$ mbar. In a programmable furnace, the tubes were heated to 1000°C in 10 h, held at 1000°C for 4 h, cooled to 850°C in 2 h, held at 850°C for 48 h, and then slowly cooled to 50°C over 48 h.

At room temperature, the fused-silica tubes were opened and the alumina crucibles were removed. The alumina crucibles were then loaded in new fused-silica tubes, covered with stainless steel frits, and sealed under a vacuum of < 10^{-4} mbar. The fused-silica tubes were replaced in a furnace that had been pre-heated to 600°C and allowed to soak for approximately one hour in order to melt the In flux. The fused-silica tubes were then removed from the furnace and centrifuged. Any remaining In flux could be removed by soaking the product in dilute HCl (1:3 H_2O), followed by gravity filtration and rinsing with H_2O and acetone. $RE_2Ru_3Ge_5$ formed as shiny black prismatic crystals in ~ 50-75% yield, depending on the rare-earth element. Other phases present in the polycrystalline product, as identified by powder X-ray diffraction, included $RERu_2Ge_2$, Ru_2Ge_3, and $RuIn_3$.

Scanning Electron Microscopy. The microprobe analyses of several crystals of each compound were performed with a Hitachi S-4700-II Scanning Electron Microscope using an EDAX Phoenix X-ray energy dispersive spectrometer (EDS). The spectrometer utilizes a Li-drifted Si detector with an ultra-thin window, and data were acquired with a beam current of 10 μA at 20 kV accelerating potential. Semi-quantitative analysis by EDS on several crystals of each composition using the *RE* L_α, Ru L_α, Ge L_α lines confirmed the 2:3:5 ratio, and also ruled out the presence of impurities such as In.

Single-Crystal X-ray Diffraction. Single crystals were selected and mounted on the tips of glass fibers for X-ray diffraction. Intensity data were collected at 298 K using ω scans on a STOE 2T imaging plate diffraction system using graphite-monochromatized Mo Kα radiation (λ = 0.71073 Å) operating at 50 kV and 40 mA with a 34 cm diameter imaging plate. Individual frames were collected with a 4 min exposure time and a 0.5° ω rotation. X-AREA, X-RED, and X-SHAPE software packages were used for data collection, integration, and analytical absorption corrections, respectively.[11] Structures were solved with the direct methods program SHELXS and refined with the full-matrix least-squares program SHELXL.[12] Each final refinement included a secondary extinction correction. The parameters for data collection and details of the structure refinements are given in Table 1. Atomic coordinates and thermal displacement parameters (U_{eq}) are given in Table 2, anisotropic thermal displacement parameters are given in Table 3, and selected interatomic distances are given in Table 4.

Intensity data for the unit cell determinations of $Sm_2Ru_3Ge_5$ were collected from 100-300 K in increments of 25 K on a STOE IPDS-II imaging plate diffraction system using graphite-

monochromatized Mo Kα radiation (λ = 0.71073 Å) operating at 50 kV and 40 mA with a 34 cm diameter imaging plate. Intensity data for the supercell of $Sm_2Ru_3Ge_5$ were collected at 175 K using ω and φ series of 0.3° scans on a Bruker Kappa APEX CCD area detector diffraction system using QuazarTM optics and Mo Kα microfocused radiation (λ = 0.71073 Å) operating at 50 kV and 1 mA. The crystal-to-detector distance was 70 mm and the exposure time was 10 sec/frame. APEX3 software package[13] was used for data collection, integration, and analytical absorption corrections. The modulated structure of $Sm_2Ru_3Ge_5$ was solved with charge flipping methods and refined with the JANA2006 program[14] using the full-matrix least-squares method.

The refinement program JANA2006 uses a periodic modulation function $p(x_4) = p(x_4 + k)$, where *k* is an integer number, to describe the changes of the basic structural parameters along the modulation vector. For a simple commensurate structure with one order of satellites, owing to the periodicity, the distortion of the position, occupancy, and displacements of a given atomic parameter x_4 of the subcell can be expressed by a periodic modulation function $p(x_4)$ in a form of a Fourier expansion:

$$p(k + x_4) = A_{sin} \sin[2\pi \cdot \mathbf{q}(k + x_4)] + A_{cos} \cos[2\pi \cdot \mathbf{q}(k + x_4)]$$

where A_{sin} is the sinusoidal coefficient of the given Fourier term, A_{cos} is the cosine coefficient, k is the lattice translation, and $\mathbf{q}$ is the modulation vector.

The diagonal vector is not consistent with orthorhombic or higher crystal symmetry. Therefore, a stable refinement for the modulated structure of $Sm_2Ru_3Ge_5$ was accomplished in the monoclinic superspace group *Pm*(α0γ)0 with eight Sm sites, ten Ru site, and fourteen Ge sites. Satellite reflections of one order were observed at 175 K and used for the refinement. One modulation wave for positional parameters was used for all atoms. Only the symmetry allowed Fourier terms of the incommensurate structure were refined. The parameters for data collection and details of the structure refinements of the modulated structure of $Sm_2Ru_3Ge_5$ are given in Table 5.

Powder X-ray Diffraction. Phase purity of the products was confirmed by laboratory powder X-ray diffraction. The samples were finely ground and mounted on a flat plate sample holder. Data was collected on a Panalytical X'pert Pro diffractometer with an Fe-filtered Cu Kα

source (λ = 1.5406 Å), operating at 45 kV and 40 mA under a continuous scanning method in the angular range 15-85° 2θ in steps of 0.0167°.

Synchrotron X-ray Diffraction. High-resolution powder X-ray diffraction data was collected at the Advanced Photon Source (APS) of Argonne National Laboratory on Sector 11-BM. Ground single crystals of $Sm_2Ru_3Ge_5$ were applied uniformly to a coating of non-diffracting grease (Dow Corning #4 electrical insulating compound) on a thin Kapton capillary. The Kapton capillary was then inserted in a slightly larger diameter Kapton capillary, before mounting in a base for the measurement. Data were collected in the temperature interval 90-300 K, at an average wavelength λ = 0.459004 Å (27 keV), while the sample was spun at 60 Hz. Rietveld refinement of the data was performed using the GSAS software package[15] and the EXPGUI interface.[16] A pseudo-Voigt peak profile function (with Finger-Cox-Jephcoat asymmetry) and the "reciprocal interpolation function" were used for modeling the diffraction peaks and the background, respectively.

Single-crystal diffraction measurements were performed on Sector 11-ID-D at the APS using an incident wavelength of 0.67 Å (18.5 keV), and on Station A2 at the Cornell High Energy Synchrotron Source (CHESS) using a wavelength of 0.22 Å (57 keV). In both experiments, a single crystal was mounted on a Kapton tube perpendicular to the incident beam and rotated at an angular speed of 1° per second over 360°. A Pilatus photon counting silicon multidetector collected frames at a rate of 10 Hz, synchronized to the sample rotation, i.e. in 0.1° steps. In order to fill in gaps between the detector chips, three sets of rotation images were collected at different detector positions, requiring less than 20 minutes in total. The resulting 3,600 images were stacked into a three-dimensional array, followed by an automated peak search to collect several hundred Bragg peaks embedded in each stack. These peaks were used to determine an orientation matrix, as well as refine the instrumental calibration, producing a good accuracy in predicting all the Bragg peak positions over the entire rotation range. The data were then transformed into reciprocal space coordinates by a software package, CCTW (Crystal Coordinate Transformation Workflow), which was developed at the APS.[17] The reciprocal space grid covered an (*hkl*) range of (±12, ±12, ±6).

Such short measurement times allowed a significant number of temperatures to be measured in a single experiment. At the APS, complete rotation scans were performed at 28 temperatures between 100 K and 300 K, including 2 K steps between 150 K and 180 K, using a

nitrogen cryoblower to control the temperature. At CHESS, measurements at 60 temperatures between 100 K and 300 K were taken with similar sample environment. In both sets of measurements, a transition from a commensurate to incommensurate structure was observed near 175 K with the growth of peaks at ($\pm q$, $\pm q$, 0), q = 0.23(1), with respect to the regular Brillouin zones. There was a slight discrepancy of ~ 2 K in the maximum of the incommensurate peak intensities measured at APS and CHESS. Since the APS maximum matched the anomaly observed in transport measurements, these were used to calibrate the CHESS data, whose temperature dependence is shown in Fig. 5.

Charge Transport Measurements. Variable-temperature four-probe resistivity and Hall effect measurements were performed on single crystals of $Sm_2Ru_3Ge_5$ with a Quantum Design Physical Property Measurement System (PPMS). The four-probe geometry was achieved with 35 μm gold wires acting as the current and voltage electrodes, attached to the crystal by conducting silver paste (DuPont 4929N). The Hall effect was measured by reversing the magnetic field H = ± 9 T. In the measurement, ρ_{xy} was taken as $\rho_{xy} = [\rho(+H) - \rho(-H)]/2$ at each point to eliminate the effect of the possible misalignment of the Hall electrodes. Both measurements were performed in the temperature range 2-300 K.

The magnetoresistance (MR) data were collected on a single crystal of $Sm_2Ru_3Ge_5$, with the same four-probe geometry as noted above. The measurement was performed on the PPMS in the temperature range 2-300 K while scanning the magnetic field from -9 T to +9 T. After the measurement, the longitudinal resistivity at a magnetic field H, $\rho(H)$, was taken as the average value of $\rho(+H)$ and $\rho(-H)$ to subtract the influence of the Hall effect. Then, $\rho(H)$ data were normalized with the formula $\Delta\rho/\rho_0 = [\rho(H)-\rho_0]/\rho_0$, where ρ_0 represents the longitudinal resistivity at zero field for each temperature.

Magnetic Measurements. A Quantum Design Magnetic Properties Measurement System (MPMS) Superconducting Quantum Interference Device (SQUID) magnetometer was used to perform dc magnetization measurements as a function of temperature and applied magnetic field. Manually selected single crystals of $Sm_2Ru_3Ge_5$ (24.5 mg) and $Pr_2Ru_3Ge_5$ (14.8 mg) were loaded in gelatin capsules that were each mounted in a separate plastic straw. Zero-field-cooled (ZFC) susceptibility data were collected in the temperature range 1.8-350 K with an applied field of 1 kOe. For $Sm_2Ru_3Ge_5$, FC and ZFC data was also collected in the temperature range 1.8-25 K with an applied field of 50 Oe. Magnetization data as a function of field, M(H),

were collected for $Sm_2Ru_3Ge_5$ with applied magnetic fields of $|H| \leq 55$ kOe at a temperature of 5 K, and for $Pr_2Ru_3Ge_5$ with $H \leq 55$ kOe at temperatures of 2 K and 300 K.

Heat Capacity. The specific heat C_p of $Sm_2Ru_3Ge_5$ and $Pr_2Ru_3Ge_5$ were measured using a relaxation technique in a Quantum Design Physical Property Measurement System (PPMS) instrument. For the measurement, several manually selected crystals were positioned on the sapphire platform of a sample puck. Thermal contact between the crystals and the platform was achieved using a thin layer of Apiezon N grease. Data was collected in the temperature range 1.8-295 K.

X-ray Absorption Near-Edge Spectroscopy (XANES). Transmission mode Sm L_{III} edge XANES measurements were performed at the Sector 20 bending magnet beamline, 20 BM, of the Advanced Photon Source at Argonne National Laboratory. The X-ray radiation was monochromatized with a Si(111) double crystal monochromator. Energy calibration was performed using an Fe foil, and the first inflection point was defined as 7110.75 eV. Harmonic contamination was minimized using a rhodium-coated X-ray mirror. To prepare samples of $Sm_2Ru_3Ge_5$ for the XANES measurement, manually selected single crystals were ground together with an appropriate amount of BN (Alfa Aesar, 99.5%) using a mortar and pestle, and the mixture was cold-pressed to form a self-supporting pellet. The measurements were performed at 20 K, 150 K, and 295 K using a closed cycle refrigerator.

Band Structure Calculations. Electronic structure calculations were performed for all three compounds using the density functional theory (DFT) plus U method[18] as implemented in the VASP *ab initio* code.[19] In the DFT part of the DFT+U total energy functional, we used the PBE flavor of the generalized gradient approximation (GGA) to the exchange and correlation functional.[20] The on-site U corrections were applied to the rare-earth *f* orbitals and to the Ru *d* orbital with the following U values: 7.4 eV for Sm, 6.5 eV for Pr, 5.6 eV for Dy, and 3.0 eV for Ru.[21] In these calculations, we fixed the lattice vectors and atom positions to their experimental values. Furthermore, we simulated these systems in ferromagnetic configurations and the self-consistent charge density optimization converged to ferromagnetic solutions with pronounced magnetic moments on the rare-earth atoms.

RESULTS AND DISCUSSION

Crystal Growth. Previously, all members of the series $RE_2Ru_3Ge_5$ (*RE* = Y, La-Nd, Sm, Gd-Tm) were reported to crystallize in the $U_2Co_3Si_5$-type structure.[10] In those cases, the materials were prepared by arc-melting stoichiometric mixtures of elements, followed by high-temperature annealing. The structures of $Y_2Ru_3Ge_5$ and $La_2Ru_3Ge_5$ were determined by single-crystal X-ray diffraction,[22] whereas the others were determined via indexing of powder X-ray diffraction data.

Rather than arc-melting, which does not lead to the new polymorph of these phases, we synthesized single crystals of $RE_2Ru_3Ge_5$ (*RE* = Pr, Sm, Dy) from a molten indium flux. A stoichiometric ratio of rare-earth element, ruthenium, and germanium is reacted in excess indium at 1000°C for 4 hours, followed by a dwell for 48 hours at 850°C, before slow cooling. The indium flux is removed from the product by way of centrifugation at 600°C, followed by soaking the crystals in dilute HCl. Shiny black prismatic crystals (Figure 1) are obtained in ~ 50-75% yield, depending on upon the rare-earth element. Crystals of $Sm_2Ru_3Ge_5$ were obtained in the highest yield with the largest dimensions, and were thus used for the majority of the characterization.

Crystal Chemistry. From single-crystal X-ray diffraction data, we determined that these three compounds crystallize in the tetragonal $Sc_2Fe_3Si_5$ structure type (Figure 2(a)). These are the first examples of germanides with this structure type. Previously, all other reported compounds with the $Sc_2Fe_3Si_5$-type structure were silicides or gallides. Other germanides within the $RE_2M_3Ge_5$ family of compounds typically assume the orthorhombic $U_2Co_3Si_5$ structure type (Figure 2(b)). The $Sc_2Fe_3Si_5$- and $U_2Co_3Si_5$-type structures are quite similar geometrically, with the difference primarily due to the bonding environments of the transition metals. In the $Sc_2Fe_3Si_5$ structure type, there are short *M*–*M* interactions along the *c* axis at a distance of approximately *c*/2; these interactions are absent in the $U_2Co_3Si_5$ structure type. As a result of these interactions, the $Sc_2Fe_3Si_5$-type structure is more "tightly" packed with a higher coordination number for some of the transition metal sites. In both structure types, the *M*(2) site possesses distorted octahedral ("4+2") coordination by main group atoms. However, in the $Sc_2Fe_3Si_5$ structure type, the *M*(1) site also exhibits a distorted octahedral bonding environment, whereas in the $U_2Co_3Si_5$ structure type, the *M*(1) site is only five-coordinate with a square pyramidal bonding environment of main group atoms.

As noted above, the entire $RE_2Ru_3Ge_5$ series was reported to crystallize with the $U_2Co_3Si_5$-type structure. However, those materials were obtained by arc-melting. It is possible that by the "low" temperature flux crystal growth method, which often allows the formation of kinetically stable phases not achievable from high temperatures, we were able to obtain the polymorphs of $Pr_2Ru_3Ge_5$, $Sm_2Ru_3Ge_5$, and $Dy_2Ru_3Ge_5$ with the $Sc_2Fe_3Si_5$ structure type. Previously, $Tb_2Ru_3Si_5$ and $Er_2Ru_3Si_5$ were reported to crystallize with polymorphs in both the $U_2Co_3Si_5$- and $Sc_2Fe_3Si_5$-type structures.[23] We should also note that with the use of the indium flux, we were also able to grow crystals of $La_2Ru_3Ge_5$, $Ce_2Ru_3Ge_5$, $Nd_2Ru_3Ge_5$, and $Tb_2Ru_3Ge_5$, all of which possessed the expected $U_2Co_3Si_5$ structure type, which will be the subject of a future publication. It is not yet clear why members of the series adopt either the $Sc_2Fe_3Si_5$-type or $U_2Co_3Si_5$-type structures, but it does not appear to simply be a matter of size (*RE* cation radius) or valence electron count.

$RE_2Ru_3Ge_5$ (*RE* = Pr, Sm, Dy) crystallize in the tetragonal space group *P*4/*mnc* with the $Sc_2Fe_3Si_5$ structure type. There are six crystallographic sites in the structure, with one *RE* atom position, two Ru atom positions, and three Ge atom positions. The site symmetries are *m*.. for *RE*, Ru(1), and Ge(1), ..2 for Ge(2), 4.. for Ge(3), and 2.22 for Ru(2). The average $Sc_2Fe_3Si_5$-type structure has previously been described in depth, so we will only provide a few brief details here. The crystal structure is a three-dimensional framework (Figure 2(a)) composed of various one-dimensional fragments that extend along the *c* axis, including extensive Ge–Ge bonding. In the current set of compounds, those fragments are $Ru(1)_4$ squares stacked to form columns (Figure 3(a)), and chains of edge-sharing $Ru(2)Ge_6$ octahedra. The Ru(1)–Ru(1) interatomic distances along the edges of the squares are ~ 2.9 Å, implying some degree of metal-metal bonding. Tunneling through the center of the $Ru(1)_4$ squares is an infinite 1D chain of Ge(3) atoms. The Ge(3)–Ge(3) chains exhibit alternating short and long distances, such as 2.850(2) Å and 3.003(2) Å for $Pr_2Ru_3Ge_5$, 2.874(2) Å and 2.903(2) Å for $Sm_2Ru_3Ge_5$, and 2.756(3) Å and 2.941(3) Å for $Dy_2Ru_3Ge_5$. Each Ru(1) atom is bonded to six Ge atoms with a distorted octahedral geometry. The Ru(2)–Ru(2) interatomic distances in the chains of $Ru(2)Ge_6$ octahedra are approximately 2.9 Å, once again suggesting metal-metal interactions. The Ge(2) atoms also form an infinite 1D chain along the *c* axis (Figure 3(b)), with interatomic distances of 2.9263(6) Å, 2.8886(6) Å, and 2.8485(5) Å for the Pr, Sm, and Dy analogues, respectively. Each Ge(2) atom is also bonded to 2 Ge(1) atoms to form alternating perpendicular Ge_3 triangles. The

RE atoms, bonded to 9 Ge atoms and 3 Ru atoms for a total coordination number of 12, are located in the cavities formed by the Ru/Ge framework.

The first indication of a structural anomaly in these compounds was observed in the room-temperature single-crystal X-ray diffraction data. The equivalent isotropic thermal displacement factor, U_{eq}, for atom Ge(2) in all three compounds (Table 2) is approximately twice that of either atom Ge(1) or Ge(3). In terms of the anisotropic displacement factors (Table 3), the U_{33} values for Ge(2) are larger than the U_{11} or U_{22} values, suggesting a cigar-shaped electron density extending along the *c* axis. Several other "235" compounds in the literature have also exhibited a peculiarity in the *X*(2) (*X* = Ga, Si, Ge) atomic site. For $Ce_2Ru_{2.31(1)}Ga_{5.69(1)}$ and $Sm_2Ru_{2.73(2)}Ga_{5.27(2)}$,[24] the Ga(2) site possesses an enlarged U_{eq} value in comparison with Ga(1) and Ga(3). However, unlike the current germanide compounds, $U_{11} = U_{22} > U_{33}$, which can be viewed as a pancake-shaped electron density. $Sm_2Ru_3Si_5$, $Sm_2(Ru,Os)_3Si_5$, and $Nd_2Os_3Si_5$ also have elevated U_{eq} values for the Si(2) atoms.[25] In the case of $Nd_2Os_3Si_5$, to account for this irregularity, the Si(2) atom was moved off the 8*g* Wyckoff position to a lower symmetry 16*i* position (*x*, *y*, *z*), and the occupancy was set at 50%. This lowered the *R* value for the structure refinement, but did not noticeably improve the U_{eq} value for the Si(2) site.

The transport and magnetic properties, as well as the heat capacity (see below), all exhibited kinks at approximately 175 K, which suggested the possibility of a structural transition near this temperature. The heat capacity measurement for $Pr_2Ru_3Ge_5$ revealed a similar kink near 200 K. Due to smaller crystal size, the transport measurements could not be performed for $Pr_2Ru_3Ge_5$. Because of smaller crystal size and much lower yield, neither the transport nor the heat capacity measurements were made for $Dy_2Ru_3Ge_5$.

Next, we collected low-temperature single-crystal X-ray diffraction on $Sm_2Ru_3Ge_5$ in order to search for a potential structural transition. Unit cell refinements in the temperature range 100-300 K did not reveal any obvious change from the room-temperature tetragonal *P*4/*mnc* structure. The *a* lattice parameter behaved as expected (Figure 4(a)), displaying an increase with temperature due to normal thermal expansion. The *c* lattice parameter, however, remained relatively constant over the entire temperature range. This may hint at some possible compressive mechanism along the *c* axis to counteract the expected normal increase from thermal expansion.

In order to obtain more precise lattice parameter data as a function of temperature, synchrotron X-ray diffraction data was collected on ground single crystals of $Sm_2Ru_3Ge_5$. The data was obtained in 10 K increments within the range 90-300 K. Once again, there was no clear indication of a structure transition. The *a* lattice parameter increases linearly over the entire temperature range, with only a very slight kink between 160 K and 170 K (Figure 4(b)). But there is more evidence for a structural abnormality over the temperature range 150-190 K in the *c* lattice parameter, which levels off, and then decreases, before increasing once again. This behavior is quite subtle, as it occurs in the third decimal place, such that the *c* axis may appear to remain relatively constant over the entire temperature range, as it did in the single-crystal X-ray diffraction data.

At this point, we performed single-crystal diffraction measurements using synchrotron X-rays at the Advanced Photon Source, over a temperature range of 100 to 300 K, with 2 K steps close to the observed transition. Below 170 K, all the observed peaks are commensurate with the tetragonal lattice, but above 170 K, we observed the sudden appearance of additional peaks at ($\pm q$, $\pm q$, 0), q = 0.23(1), with respect to the commensurate (*hkl*) Bragg peaks representing an incommensurate modulation of the parent structure (Figure 5). These peaks were observed around every integer (*hkl*) value in the measured range with the exception of some systematic absences. For example, there is a modulation of the intensities along the (*h*00) direction, with strong peaks at h = 8 and 12, but no peaks at h = 6 and 10. We performed a more detailed investigation of the temperature dependence of this incommensurate modulation at CHESS. The intensity of these peaks has a maximum at approximately 175 K, the temperature of the transport anomalies, above which it falls rapidly (Figure 6). At 190 K, diffuse features are still observed at the same wavevectors, but the modulation is only short-range above this temperature, with a significant tail in the intensity extending above 210 K.

We were not able to perform a complete structure solution of the modulated structure using the synchrotron data because of significant fluorescent background in the APS data at 18.5 keV. Subsequently, we obtained single-crystal X-ray diffraction data in-house so as to be able to refine the structure using the JANA2006 software. This confirmed the observations from the synchrotron data and revealed that the incommensurate structure of $Sm_2Ru_3Ge_5$ contains weak positionally modulated atoms. The Ge(11) and Ge(13) atoms in the zig-zag chains of Ge were found to distort the most from their average position (Figure 7). The displacement between the

Ge(11)-Ge(11) and Ge(13)-Ge(13) atoms along the *b* axis is around 0.22 Å while the displacements along the *a* and *c* axes are less than 0.02 Å The small displacement of all other atoms from their average positions is around 0.03 Å. The shortest distance between two Ge atoms is 2.666(4) Å and the longest is 2.917(3) Å. The shortest Sm-Ge distance is 2.828(3) Å and the longest is 3.32(1) Å, and the shortest and longest Ru-Ge distances are 2.479(4) Å and 2.583(4) Å, respectively.

Transport Properties. The temperature dependence of the electrical resistivity (both cooling and warming processes) for $Sm_2Ru_3Ge_5$ is shown in Figure 8. At ~ 175 K, a jump occurs in the resistivity curve; this jump corresponds to the CDW transition observed in the single-crystal and powder X-ray diffraction experiments. Near the transition, some hysteresis is observed between the resistivity on heating versus cooling; this becomes more pronounced as the rate of heating or cooling is increased. Similar resistivity behavior with a rapid jump and hysteresis is reported for the CDW materials $Lu_2Ir_3Si_5$ and $Er_2Ir_3Si_5$.[26]

Above the transition temperature, the resistivity displays thermally-activated behavior, indicating that above 175 K, $Sm_2Ru_3Ge_5$ is a conventional semiconductor. The thermally-activated behavior disappears below the transition temperature, but the resistivity continues rising with the decrease in temperature until a broad maximum near 90 K. Below 90 K, the resistivity decreases gradually, reaching a minimum at ~ 29 K. As the temperature falls below 29 K, the resistivity experiences an upturn, and at 6.2 K, a sharp peak corresponding to the ferromagnetic ordering (see below) is observed. The resistivity minimum at 29 K, and the upturn in resistivity at lower temperatures are indicative of the Kondo effect. Similar low-temperature resistivity behavior was exhibited by the Kondo lattice compound $CePd_{1-x}Bi_2$.[27]

To better understand the novel resistivity behavior for $Sm_2Ru_3Ge_5$, we also performed Hall effect measurements. The inset of Figure 9(a) displays the magnetic field dependence of the Hall resistivity (ρ_{xy}) at various temperatures. Extracting the slope of the magnetic field dependence of the Hall resistivity, the Hall coefficient (R_H) is obtained as a function of temperature (Figure 9(a)). We observe that the Hall coefficient is negative over the entire temperature range, indicating that electrons are the dominant carriers in $Sm_2Ru_3Ge_5$. Furthermore, the Hall coefficient also exhibits strong temperature dependence, particularly at low temperature. Using the equation $R_H = 1/ne$, it is possible to calculate the electron concentration as a function of temperature (Figure 9(b)) under the assumption that only a single

band contributes to the transport behavior. From the temperature dependence, an anomaly occurs at approximately the CDW transition temperature (shown by the dashed black line). Above the transition temperature, the electron concentration varies almost linearly with temperature, and extrapolates to zero (shown by the dashed red line). This suggests that the electron concentration is affected only by thermal activation, and that the band gap does not change with temperature. However, below the transition temperature, the electron concentration obeys a power law. As the band gap becomes narrower, more thermally "activated" carriers emerge. The power-law-like behavior implies that the band gap becomes wider with decreasing temperature. The band gap may be opened wider by the Kondo effect at low temperatures. Based upon the analysis of the electrical resistivity and electron concentration, we conclude that $Sm_2Ru_3Ge_5$ exhibits a conventional semiconductor to Kondo semiconductor transition that happens simultaneously with the CDW transition.

The magnetoresistance (MR) is a powerful tool for investigating the properties of electronic scattering, and has proven important in the research of density wave systems.[28] Magnetic field dependence of MR for $Sm_2Ru_3Ge_5$ at various temperatures is shown in Figure 10(a). A moderate MR effect of up to 19% under a field of 9 T at 2 K is exhibited by $Sm_2Ru_3Ge_5$, while at high temperatures, the magnetoresistance is negligible. The magnetoresistance under a field of 9 T at various temperatures is plotted in Figure 10(b). From the data, a sign reversal in MR is observed at the CDW transition temperature (~ 175 K). This is consistent with the results of the other charge transport measurements, and provides additional evidence for the CDW transition.

Magnetic Properties. Magnetic data was collected on single crystals of $Sm_2Ru_3Ge_5$ and $Pr_2Ru_3Ge_5$. Sufficient quantity of phase-pure single crystals of $Dy_2Ru_3Ge_5$ could not be obtained for an accurate determination of the magnetic properties. The magnetic susceptibility (χ_m) and inverse magnetic susceptibility ($1/\chi_m$) of $Sm_2Ru_3Ge_5$ over the temperature range 1.8-350 K are shown in Figure 11(a). A clear ferromagnetic transition is observed at T_c = 7 K. The weak, almost linear magnetic susceptibility above the ferromagnetic transition is consistent with van Vleck paramagnetism, which is common in Sm-containing compounds. The small saturation moment (Figure 11(b)) results from the thermal population of the closely spaced upper Hund's rule multiplet in the Sm^{3+} cation.

The magnetic susceptibility (χ_m) and inverse magnetic susceptibility ($1/\chi_m$) of $Pr_2Ru_3Ge_5$ over the temperature range 1.8-350 K are shown in Figure 12(a). There appears to possibly be antiferromagnetic ordering just below 1.8 K, but because this is the current limit of our measurement capabilities, this cannot be confirmed. The feature in the magnetic susceptibility at 14.6 K may signify antiferromagnetic ordering obscured by the averaging of the different orientations of the crystals, or even possibly some complex incommensurate order. At high temperatures, $Pr_2Ru_3Ge_5$ exhibits typical paramagnetic behavior. A Curie-Weiss fitting to the magnetic susceptibility data above 150 K yields a Curie constant C = 1.616(3) emu K mol^{-1} and a Weiss constant θ_p = 17.8(5) K. The effective magnetic moment, as determined from the equation $\mu_{eff} = 2.828C^{1/2}$, is 3.594(6) μ_B/Pr. This value is approximately equal to the calculated effective magnetic moment (3.58 μ_B) for the Pr^{3+} cation.[29] Magnetic isotherms, M(H), measured at 2 K and 300 K are presented in Figure 12(c).

Heat Capacity. The specific heat of $Sm_2Ru_3Ge_5$ was measured over the temperature range 1.8-295 K. There are two sharp peaks in the heat capacity, one occurring at ~ 7 K, corresponding to the ferromagnetic transition, and a second one just below 175 K, which is coincident with the CDW transition. In the low temperature regime (T < 25 K), the heat capacity, C, is composed of electron, phonon, and magnon contributions (Figure 13(a)). The electron and phonon contributions can be determined according to the Debye model, $C(T) = \gamma T + \beta T^3$. From a linear fit to the C/T versus T^2 plot (Figure 13(b)), values of 0.0181(5) J mol^{-1} Sm^{3+} K^{-2} and 0.000508(1) J mol^{-1} Sm^{3+} K^{-4} are calculated for γ and β, respectively. The Debye temperature, Θ_D, can be obtained using the formula $\Theta_D = [12\pi^4 NR/(5\beta)]^{1/3}$, where N is the number of atoms in the empirical chemical formula, and R is the ideal gas constant (8.314 J mol^{-1} K^{-1}). We are able to calculate a value of Θ_D = 337.0(2) K for $Sm_2Ru_3Ge_5$. The magnon contribution to the total specific heat can then be determined by subtracting the electron and phonon contributions from the total specific heat. The magnetic entropy, S_{magnon}, can be calculated from the equation $S_{magnon} = \int C_{magnon}/T dT$. This yields a value of S_{magnon} = 5.13 J mol^{-1} Sm^{3+} K^{-1}.

In the high temperature regime (T > 50 K), the specific heat of $Sm_2Ru_3Ge_5$ no longer follows a simple Debye model (Figure 13(c)). The electron and phonon contributions can be fit to the experimental data using a polynomial. By subtracting the electron and phonon contributions from the total specific heat, we are able to determine the contribution supplied by

the charge density wave (C_{CDW}). The entropy of the charge density wave, S_{CDW}, can then be calculated, providing a value of 1.30 J mol^{-1} Sm^{3+} K^{-1}.

The specific heat of $Pr_2Ru_3Ge_5$ was also measured within the temperature interval 1.8-295 K (Figure 13(d)). There are no features observed in the low temperature range, but once again, a peak is observed at high temperature, just below 200 K. This suggests that in analogy to $Sm_2Ru_3Ge_5$, $Pr_2Ru_3Ge_5$ also exhibits CDW behavior. Once again, the electron and phonon contributions to the specific heat can be determined via a polynomial fitting. Subsequently, the entropy of the charge density wave in $Pr_2Ru_3Ge_5$ is calculated to be S_{CDW} = 2.34 J mol^{-1} Pr^{3+} K^{-1}. The larger entropy for the Pr analog implies a more significant structure modulation when the CDW forms.

XANES. Measurements were carried out to probe if $Sm_2Ru_3Ge_5$ exhibited temperature dependent valence fluctuations. The general appearance of the Sm L_{III} edge XANES is a useful fingerprint for the valence state of Sm. Both Sm^{2+} and Sm^{3+} exhibit intense white line resonances at threshold energies, which are separated by ~ 7 eV. Hence, in mixed-valent Sm compounds, two white line features are observed.[30] For all temperatures, the spectrum of $Sm_2Ru_3Ge_5$ is characterized by a single intense white line resonance, and the curves largely overlap (Figure 14). This indicates that, to within the accuracy of the measurements, the sample does not exhibit valence changes down to 20 K.

Band Structure. The GGA+U orbital projected density of states (PDOS) of $Pr_2Ru_3Ge_5$, $Sm_2Ru_3Ge_5$, and $Dy_2Ru_3Ge_5$ are shown in Figure 15, and the electron bands near the Fermi level (E_F) are plotted in Figure 16. These calculations indicate that all three compounds are metallic. It should be noted that because the calculations have been performed using the average structures of these compounds, they do not reflect the presence of the CDW, and therefore suggest metallic properties. The crystal structure distortion occurs below T_{CDW}, which drives the gap opening and the subsequent semiconducting properties observed in the charge transport measurements for $Sm_2Ru_3Ge_5$. $Sm_2Ru_3Ge_5$ exhibits a unique situation where the spin-up Sm *f* peak is located in the empty states near E_F, but close enough to the Fermi level to produce a manifold of *f* bands that extend in part to the filled states near E_F. The proximity of the *f* band to the Fermi level causes the Kondo behavior observed at temperatures below the CDW transition.

The largest contribution to the filled states near E_F originates from the Ru *d* orbitals, with a smaller contribution from the partially filled Ge *p* orbitals. The DOS components originating

from the Ru *d* orbitals decrease near the Fermi level, where it starts increasing again to form a dome-like feature smaller than that found in the filled states near E_F. Multiple bands cross the Fermi level not only in the direction of the reciprocal space parallel to the chains, but also in the perpendicular direction. An inspection of the Ru *d* projected DOS resolved by symmetry of the d orbital shows that the predominant contribution to the DOS, and therefore to the bands crossing the Fermi level, comes from the d_{xz}, d_{yz}, and d_{z^2} orbitals with *z* taken parallel to the tetragonal *c* axis. This reflects the fact that the closest contacts between Ru atoms occur in dimers that are oriented along both the in- and out-of-plane directions. These dimers are connected by Ge atoms along both the *c* axis and *ab* plane, and these links favor band dispersion both along the Ge chains, as well as perpendicular to the chains.

CONCLUSIONS

We discovered new polymorphs of the $RE_2Ru_3Ge_5$ (*RE* = Pr, Sm, Dy) compounds, and showed that they harbor a unique type of CDW. This is manifested at low-temperature structure and defines a new class of charge density wave ordering. The discovery of a CDW in these materials with the $Sc_2Fe_3Si_5$ structure type implies that similar CDWs may exist in analogous germanides, silicides, and gallides, suggesting that they deserve to be reinvestigated.

Transport measurements and heat capacity confirm the onset of CDW behavior in $RE_2Ru_3Ge_5$ (*RE* = Pr, Sm, Dy). It would be beneficial to further study these materials by selected area electron diffraction, angle-resolved photoemission spectroscopy, and scanning tunneling microscopy in order to better elucidate the ordering mechanism. Furthermore, analogous to the iron arsenide superconductors, it would be interesting to see if the CDW order can be suppressed via doping or pressure so as to induce superconductivity. This would not be unexpected, as a number of other isostructural compounds display superconductivity, including the series $RE_2Fe_3Si_5$ (*RE* = Sc, Y, Tm, Lu).[31]

ASSOCIATED CONTENT

Supporting Information

Crystallographic data in CIF format. This material is available free of charge via the Internet at http://pubs.acs.org.

AUTHOR INFORMATION

Corresponding Author

*E-mail: m-kanatzidis@northwestern.edu. Tel: 847-467-1541. Fax: 847-491-5937.

Notes

The authors declare no competing financial interest.

ACKNOWLEDGMENT

Work at Argonne National Laboratory was supported by the U.S. Department of Energy, Office of Science, Materials Sciences and Engineering. Use of the Advanced Photon Source and the Center for Nanoscale Materials, including the Electron Microscopy Center, at Argonne National Laboratory was supported by the U.S. Department of Energy, Office of Science, Office of Basic Energy Sciences, under Contract No. DE-AC02-06CH11357. Sector 20 operations at the Advanced Photon Source were supported by the U.S. Department of Energy and the Canadian Light Source. Single-crystal X-ray diffraction work (modulated structure at 175 K) made use of the Integrated Molecular Structure Education and Research Center (IMSERC) at Northwestern University, which has received support from the Soft and Hybrid Nanotechnology Experimental (SHyNE) Resource (NSF NNCI-1542205), the State of Illinois, and the International Institute for Nanotechnology (IIN). Research conducted at the Cornell High Energy Synchrotron Source (CHESS) was supported by the National Science Foundation and the National Institute of Health/National Institute of General Medical Sciences under NSF award DMR-1332208. Work at the Ames Laboratory was supported by the US Department of Energy, Basic Energy Sciences, Division of Materials Sciences and Engineering under Contract No. DE-AC02-07CH11358.

Computational work was done using resources of the National Energy Research Scientific Computing Center (NERSC), a U.S. Department of Energy Office of Science User Facility, supported by the U.S. Department of Energy, Office of Science, under Contract No. DE-AC02-05CH11231. We would like to thank Saul Lapidus for his assistance during the data collection at Sector 11-BM of the APS, Omar Chmaissem for his aid with the synchrotron single-crystal X-ray diffraction measurements, and Justin Wozniak for this assistance with the processing of the synchrotron single-crystal X-ray diffraction data.

REFERENCES

(1) (a) Malliakas, C.; Billinge, S.J.L.; Kim, H.J.; Kanatzidis, M.G. *J. Am. Chem. Soc.* **2005**, *127*, 6510. (b) Malliakas, C.D.; Kanatzidis, M.G. *J. Am. Chem. Soc.* **2006**, *128*, 12612. (c) Malliakas, C.D.; Iavarone, M.; Fedor, J.; Kanatzidis, M.G. *J. Am. Chem. Soc.* **2008**, *130*, 3310. (d) Malliakas, C.D.; Kanatzidis, M.G. *J. Am. Chem. Soc.* **2007**, *129*, 10675. (e) Malliakas, C.D.; Kanatzidis, M.G. *J. Am. Chem. Soc.* **2009**, *131*, 6896.

(2) Malliakas, C.D.; Kanatzidis, M.G. *J. Am. Chem. Soc.* **2013**, 1719.

(3) (a) Zhuravleva, M.A.; Evain, M.; Petricek, V.; Kanatzidis, M.G. *J. Am. Chem. Soc.* **2007**, *135*, 3082. (b) Gray, D.L.; Francisco, M.C.; Kanatzidis, M.G. *Inorg. Chem.* **2008**, *47*, 7243.

(4) Manuel, P.; Chapon, L.C.; Todorov, I.S.; Chung, D.Y.; Castellan, J.-P.; Rosenkranz, S.; Osborn, R.; Toledano, P.; Kanatzidis, M.G. *Phys. Rev. B* **2010**, *81*, 184402.

(5) Rotter, M.; Tegel, M.; Johrendt, D.; Schellenberg, I.; Hermes, W.; Pöttgen, R. *Phys. Rev. B* **2008**, *78*, 020503.

(6) (a) Cortes-Gil, R.; Parker, D.R.; Pitcher, M.J.; Hadermann, J.; Clarke, S.J. *Chem. Mater.* **2010**, *22*, 4304. (b) Rotter, M.; Tegel, M.; Johrendt, D. *Phys. Rev. Lett.* **2008**, *101*, 107006.

(7) Sefat, A.S.; Jin, R.; McGuire, M.A.; Sales, B.C.; Singh, D.J.; Mandrus, D. *Phys. Rev. Lett.* **2008**, *101*, 117004. (b) Li, L.J.; Luo, Y.K.; Wang, Q.B.; Chen, H.; Ren, Z.; Tao, Q.; Li, Y.K.; Lin, X.; He, M.; Zhu, Z.W.; Cao, G.H.; Xu, Z.A. *New J. Phys.* **2009**, *11*, 025008.

(8) Jiang, S.; Xing, H.; Xuan, G.; Wang, C.; Ren, Z.; Feng, C.; Dai, J.; Xu, Z.; Cao, G. *J. Phys.: Condens. Matter* **2009**, *21*, 382203.

(9) Alireza, P.L.; Ko, Y.T.C.; Gillet, J.; Petrone, C.M.; Cole, J.M.; Lonzarich, G.G.; Sebastian, S.E. *J. Phys.: Condens. Matter* **2009**, *21*, 012208.

(10) Venturini, G.; Méot-Meyer, M.; Marêché, J.F.; Malaman, B.; Roques, B. *Mater. Res. Bull.* **1986**, *21*, 33.

(11) *X-AREA, X-SHAPE, and X-RED*; STOE and Cie GmbH: Darmstadt, Germany, **2009**.

(12) Sheldrick, G. *Acta Crytallogr., Sect. A: Found. Crystallogr.* **2008**, *64*, 112.

(13) *APEX3*; Bruker AXS, Inc.: Madison, Wisconsin, **2016**.

(14) Petrícek, V.; Dusek, M.; Palatinus, L. *Z. Kristallogr. – Cryst. Mater.* **2014**, *229*, 345.

(15) *General Structure Analysis System (GSAS)*; A.C. Larson and R.B. von Dreele, Los Alamos National Laboratory: Los Alamos, New Mexico, **2004**.

(16) Toby, B.H. *J. Appl. Crystallogr.* **2001**, *34*, 210.

(17) https://www1.aps.anl.gov/science/scientific-software/cctw

(18) (a) Liechtenstein, A.I.; Anisimov, V.I.; Zaanen, J. *Phys. Rev. B* **1995**, *52*, R5467. (b) Anisimov, V.I.; Aryasetiawan, F.; Liechtenstein, A.I. *J. Phys.: Condens. Matter* **1997**, *9*, 767. (c) Dudarev, S.L.; Botton, G.A.; Savrasov, S.Y.; Humphreys, C.J.; Sutton, A.P. *Phys. Rev. B* **1998**, *57*, 1505.

(19) (a) Kresse, G.; Furthmuller, J. *Comput. Mater. Sci.* **1996**, *6*, 15. (b) Kresse, G.; Joubert, D. *Phys. Rev. B* **1999**, *59*, 1758.

(20) Perdew, J.P.; Burke, K.; Ernzerhof, M. *Phys. Rev. Lett.* **1996**, *77*, 3865.

(21) Setyawan, W.; Curtarolo, S. *Computational Materials Science* **2010**, *49*, 299.

(22) Venturini, G.; Malaman, B.; Roques, B. *J. Less-Common Met.* **1989**, *152*, 51.

(23) Paccard, D.; Paccard L. *J. Less-Common Met.* **1990**, *163*, L13.

(24) Jeitschko, W.; Schlüter, M. *Z. Anorg. Allg. Chem.* **2010**, *636*, 1100.

(25) (a) Salamakha, P.; Sologub, O.; Bocelli, G.; Righi, L. *J. Alloys Compd.* **2000**, *299*, L6. (b) Rizzoli, C.; Sologub, O.L.; Salamakha, P.S. *J. Alloys Compd.* **2002**, *337*, L4. (c) Rizzoli, C.; Salamakha, P.S.; Sologub, O.L.; Belleti, D.; Gonçalves, A.P.; Almeida, M. *J. Alloys Compd.* **2004**, *363*, 217.

(26) (a) Kuo, Y.K.; Sivakumar, K.M.; Su, T.H.; Lue, C.S. *Phys. Rev. B* **2006**, *74*, 045115. (b) Lee, M.H.; Chen, C.H.; Chu, M.-W.; Lue, C.S.; Kuo, Y.K. *Phys. Rev. B* **2011**, *83*, 155121. (c) Padam, R.; Thamizhavel, A.; Ravi, S.; Ramakrishnan, S.; Pal, D. *AIP Conf. Proc.* **2012**, *1447*, 1007.

(27) Han, F.; Wan, X.; Phelan, D.; Stoumpos, C.S.; Sturza, M.; Malliakas, C.D.; Li, Q.; Han, T.-H.; Zhao, Q.; Chung, D.Y.; Kanatzidis, M.G. *Phys. Rev. B* **2015**, *92*, 045112.

(28) Han, F.; Zhu, X.; Mu, G.; Cheng, P.; Wen, H.-H. *Phys. Rev. B* **2008**, *78*, 180503.

(29) Kittel, C. *Introduction to Solid State Physics*, 8th ed.; John Wiley & Sons, Inc.: Hoboken, New Jersey, 2005.

(30) Beaurepaire, E.; Kappler, J.P.; Krill, G. *Phys. Rev. B* **1990**, *41*, 6768.

(31) (a) Braun, H.F. *Phys. Lett.* **1980**, *75A*, 386. (b) Segre, C.U.; Braun, H.F. *Phys. Lett.* **1981**, *85A*, 372.

Table 1. Structure Refinement Details from Single-Crystal X-ray Diffraction for $RE_2Ru_3Ge_5$ compounds[a]

	$Pr_2Ru_3Ge_5$	$Sm_2Ru_3Ge_5$	$Dy_2Ru_3Ge_5$
formula weight	947.98	966.86	991.16
a (Å)	11.020(2)	10.982(2)	10.927(2)
c (Å)	5.853(1)	5.777(1)	5.697(1)
volume (Å^3)	710.7(2)	696.7(2)	680.2(2)
ρ_c (g/cm^3)	8.859	9.218	9.678
μ (mm^{-1})	40.307	43.989	49.759
F(000)	1640	1664	1696
crystal size (mm)	0.170 x 0.160 x 0.140	0.130 x 0.096 x 0.072	0.100 x 0.099 x 0.050
θ range for data collection (deg)	3.94 to 38.16	3.71 to 34.99	3.73 to 33.00
index ranges	$-17 \le h \le 19$ $-19 \le k \le 19$ $-10 \le l \le 8$	$-17 \le h \le 15$ $-17 \le k \le 17$ $-8 \le l \le 9$	$-16 \le h \le 16$ $-16 \le k \le 16$ $-8 \le l \le 8$
reflections collected	12320	10006	8580
independent reflections	1044 [R_{int} = 0.0571]	828 [R_{int} = 0.0340]	703 [R_{int} = 0.0522]
completeness to θ = 34.90°	99.3%	99.3%	99.6%
data / restraints / parameters	1044 / 0 / 31	828 / 0 / 31	703 / 0 / 31
GOF	1.565	1.466	1.269
final R indices [$>2\sigma(I)$][b]	R_{obs} = 0.0280 wR_{obs} = 0.0677	R_{obs} = 0.0291 wR_{obs} = 0.0680	R_{obs} = 0.0292 wR_{obs} = 0.0685
R indices [all data][b]	R_{all} = 0.0281 wR_{all} = 0.0677	R_{all} = 0.0293 wR_{all} = 0.0681	R_{all} = 0.0293 wR_{all} = 0.0686

[a] For all structures, λ = 0.71073 Å, temperature is 298(2) K, space group is $P4/mnc$, and Z = 4.

[b] $R = \Sigma \, ||F_o| - |F_c|| \, / \, \Sigma \, |F_o|$, $wR = \{\Sigma \, [w(|F_o|^2 - |F_c|^2)^2] \, / \, \Sigma \, [w(|F_o|^4)]\}^{1/2}$ and calc $w = 1 \, / \, [\sigma^2(F_o^2) + (A \times P)^2 + (B \times P)]$ where $P = (F_o^2 + 2F_c^2) \, / \, 3$. For $Pr_2Ru_3Ge_5$, A = 0.0137 and B = 9.5663. For $Sm_2Ru_3Ge_5$, A = 0.0196 and B = 15.7594. For $Dy_2Ru_3Ge_5$, A = 0.0228 and B = 15.6279.

Table 2. Atomic Coordinates and Equivalent Isotropic Displacement Parameters ($Å^2 \times 10^3$) for $RE_2Ru_3Ge_5$ compounds

	Wyckoff	*x*	*y*	*z*	U_{eq}[a]
Pr	8*h*	0.2644(1)	0.4300(1)	0	7(1)
Ru(1)	8*h*	0.1432(1)	0.1233(1)	0	6(1)
Ru(2)	4*d*	0	0.5	0.25	5(1)
Ge(1)	8*h*	0.0280(1)	0.3195(1)	0	6(1)
Ge(2)	8*g*	0.1758(1)	0.6758(1)	0.25	12(1)
Ge(3)	4*e*	0	0	0.2435(2)	6(1)
Sm	8*h*	0.2639(1)	0.4303(1)	0	5(1)
Ru(1)	8*h*	0.1426(1)	0.1228(1)	0	4(1)
Ru(2)	4*d*	0	0.5	0.25	4(1)
Ge(1)	8*h*	0.0299(1)	0.3190(1)	0	4(1)
Ge(2)	8*g*	0.1763(1)	0.6763(1)	0.25	8(1)
Ge(3)	4*e*	0	0	0.2512(2)	4(1)
Dy	8*h*	0.2638(1)	0.4302(1)	0	13(1)
Ru(1)	8*h*	0.1424(1)	0.1228(1)	0	11(1)
Ru(2)	4*d*	0	0.5	0.25	11(1)
Ge(1)	8*h*	0.0317(1)	0.3188(1)	0	11(1)
Ge(2)	8*g*	0.1763(1)	0.6763(1)	0.25	17(1)
Ge(3)	4*e*	0	0	0.2581(2)	11(1)

[a] U_{eq} is defined as one third of the trace of the orthogonalized U_{ij} tensor.

Table 3. Anisotropic Displacement Parameters ($Å^2 \times 10^3$) for $RE_2Ru_3Ge_5$ compounds [a]

	U_{11}	U_{22}	U_{33}	U_{12}	U_{13}	U_{23}
Pr	5(1)	8(1)	6(1)	0(1)	0	0
Ru(1)	5(1)	5(1)	7(1)	0(1)	0	0
Ru(2)	6(1)	6(1)	4(1)	1(1)	0	0
Ge(1)	6(1)	5(1)	6(1)	0(1)	0	0
Ge(2)	9(1)	9(1)	17(1)	-2(1)	-6(1)	6(1)
Ge(3)	6(1)	6(1)	6(1)	0	0	0
Sm	4(1)	7(1)	4(1)	0(1)	0	0
Ru(1)	3(1)	4(1)	6(1)	0(1)	0	0
Ru(2)	5(1)	5(1)	2(1)	1(1)	0	0
Ge(1)	4(1)	4(1)	4(1)	0(1)	0	0
Ge(2)	7(1)	7(1)	11(1)	-1(1)	-5(1)	5(1)
Ge(3)	4(1)	4(1)	3(1)	0	0	0
Dy	9(1)	13(1)	16(1)	0(1)	0	0
Ru(1)	8(1)	8(1)	16(1)	0(1)	0	0
Ru(2)	10(1)	10(1)	12(1)	1(1)	0	0
Ge(1)	10(1)	8(1)	15(1)	0(1)	0	0
Ge(2)	13(1)	13(1)	23(1)	-2(1)	-5(1)	5(1)
Ge(3)	9(1)	9(1)	14(1)	0	0	0

[a] The anisotropic displacement factor exponent takes the form: $-2\pi^2[h^2a^{*2}U_{11} + ... + 2hka^*b^*U_{12}]$.

Table 4. Selected Interatomic Distances (Å) for $RE_2Ru_3Ge_5$ compounds

	RE = Pr	*RE* = Sm	*RE* = Dy
RE–Ge(1)	2.8752(9)	2.846(1)	2.814(1)
RE–Ge(3) x2	3.0968(7)	3.0617(8)	3.0235(8)
RE–Ge(1) x2	3.1035(6)	3.0600(6)	3.0168(6)
RE–Ge(2) x2	3.2283(8)	3.2084(9)	3.1875(9)
RE–Ge(2) x2	3.2299(6)	3.2112(6)	3.1890(6)
RE–Ru(1) x2	3.2780(6)	3.2453(6)	3.2062(6)
RE–Ru(2)	3.3505(5)	3.3273(5)	3.3043(5)
Ru(1)–Ge(1)	2.5071(9)	2.484(1)	2.459(1)
Ru(1)–Ge(3) x2	2.5238(8)	2.5259(9)	2.5091(7)
Ru(1)–Ge(2) x2	2.5400(6)	2.5265(7)	2.527(1)
Ru(1)–Ge(1)	2.5601(9)	2.562(1)	2.562(1)
Ru(1)···Ru(1) x2	2.9458(8)	2.9235(9)	2.906(1)
Ru(2)–Ge(1) x4	2.4887(6)	2.4793(7)	2.4638(8)
Ru(2)–Ge(2) x2	2.7397(9)	2.739(1)	2.724(1)
Ru(2)···Ru(2) x2	2.9263(6)	2.8886(6)	2.8485(5)
Ge(1)–Ge(2) x2	2.6814(8)	2.6864(9)	2.682(1)
Ge(2)–Ge(2) x2	2.9263(6)	2.8886(6)	2.8485(5)
Ge(3)–Ge(3)	2.850(2)	2.874(2)	2.756(3)
Ge(3)–Ge(3)	3.003(2)	2.903(2)	2.941(3)

Table 5. Structure Refinement Details from Single-Crystal X-ray Diffraction for the Modulated Structure of Sm_2Ru_3Ge[a]

formula weight	966.86
temperature (K)	100
λ (Å)	0.71073
crystal system	monoclinic
space group	$Pm(\alpha 0 \gamma)0$
a (Å)	10.9955(2)
b (Å)	5.7823(3)
c (Å)	10.9942(3)
$\alpha = \beta = \gamma$ (°)	90
q-vector	$0.219(5)a^* + 0.219(4)c^*$
volume (Å^3)	699.00(4)
Z	4
ρ_c (g/cm^3)	9.1887
μ (mm^{-1})	43.845
F(000)	1664
crystal size (mm)	0.066 x 0.050 x 0.044
θ range for data collection (deg)	0.57 to 45.81
index ranges	$-22 \le h \le 22$, $-11 \le k \le 11$, $-21 \le l \le 22$, $1 \le m \le 1$
reflections collected	70542 (20975 main + 49567 satellites)
independent reflections	17468 (9369 main + 19816 satellites) [R_{int} = 0.0611]
completeness to θ = 41.78°	98%
data / restraints / parameters	17468 / 3 / 0 / 617
GOF	2.05
final R indices [>2σ(I)][a]	R_{obs} = 0.0636, wR_{obs} = 0.1723
R indices [all data][a]	R_{all} = 0.0813, wR_{all} = 0.1752
final R main indices [>2σ(I)][a]	R_{obs} = 0.0607, wR_{obs} = 0.1703
R main indices [all data][a]	R_{all} = 0.0609, wR_{all} = 0.1704
final R 1st order satellites [>2σ(I)][a]	R_{obs} = 0.1207, wR_{obs} = 0.2411
R 1st order satellites [all data][a]	R_{all} = 0.2730, wR_{all} = 0.3011
final R indices [>2σ(I)][a]	R_{obs} = 0.0636 wR_{obs} = 0.1723
R indices [all data][a]	R_{all} = 0.0813 wR_{all} = 0.1752

[a] $R = \Sigma \, ||F_o| - |F_c|| \, / \, \Sigma \, |F_o|$, $wR = \{\Sigma \, [w(|F_o|^2 - |F_c|^2)^2] \, / \, \Sigma \, [w(|F_o|^4)]\}^{1/2}$ and calc $w = 1 \, / \, [\sigma^2(F_o^2) + 0.0016 \times I^2]$.

Figure 1. SEM micrographs of typical crystals of (a) $Pr_2Ru_3Ge_5$, (b) $Sm_2Ru_3Ge_5$, and (c) $Dy_2Ru_3Ge_5$. Some surface etching of the crystals due to soaking in dilute HCl is visible.

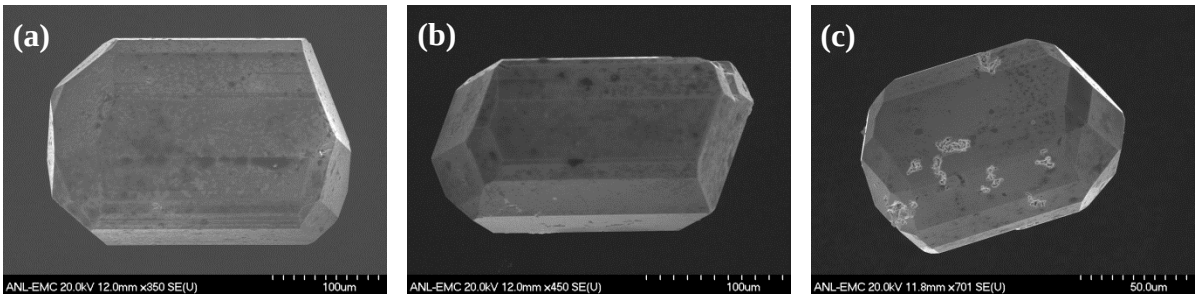

Figure 2. (a) Tetragonal $Sc_2Fe_3Si_5$-type crystal structure as viewed along the *c* axis. (b) Orthorhombic $U_2Co_3Si_5$-type crystal structure as viewed along the *c* axis. Rare-earth or actinide elements, transition metals, and main group elements (Ga, Ge, Si) are shown as black, blue, and green spheres, respectively.

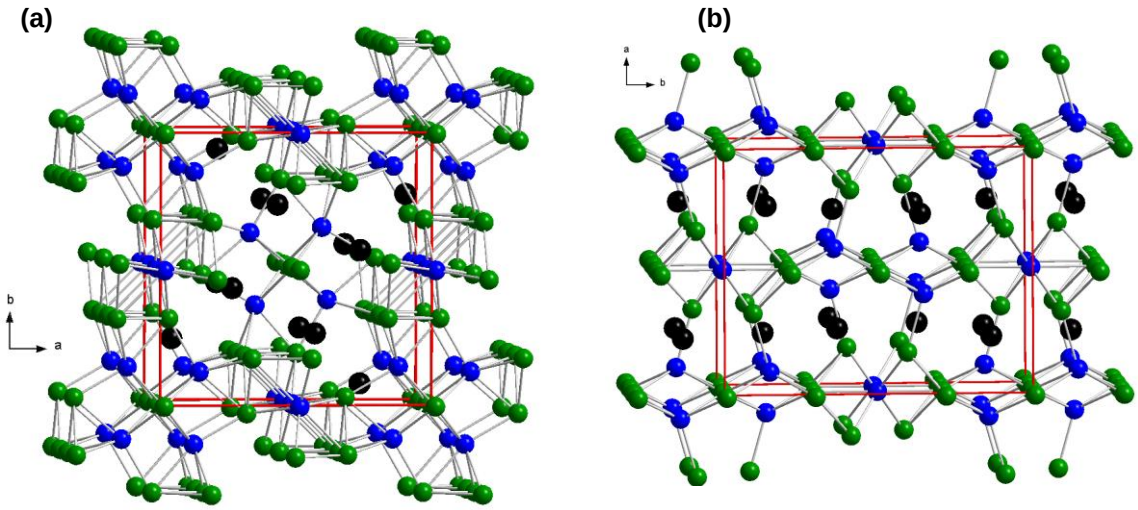

Figure 3. (a) In $RE_2Ru_3Ge_5$ (*RE* = Pr, Sm, Dy), a view of the $Ru(1)_4$ squares surrounding an infinite 1D chain of Ge(3) atoms. The Ru(1)–Ru(1) metal "bonding" is shown with thin dotted lines. (b) View of the infinite 1D chains of Ge(1) and Ge(2) atoms, with each link in the chain consisting of a Ge_3 triangle. Ru and Ge atoms are shown as blue and green spheres, respectively.

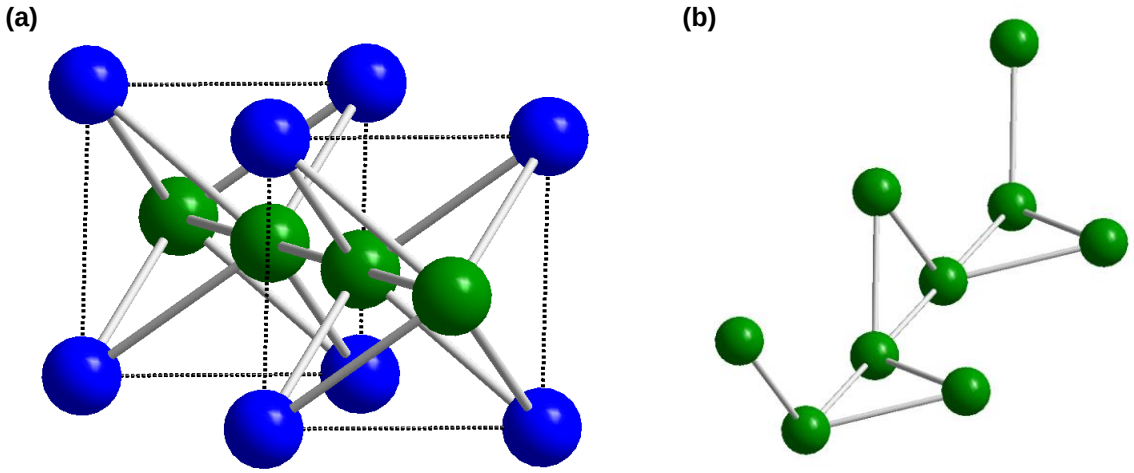

Figure 4. (a) Lattice parameters versus temperature for $Sm_2Ru_3Ge_5$, as determined from (a) unit cell refinements of single-crystal X-ray diffraction data and (b) Rietveld refinements of synchrotron powder X-ray diffraction data.

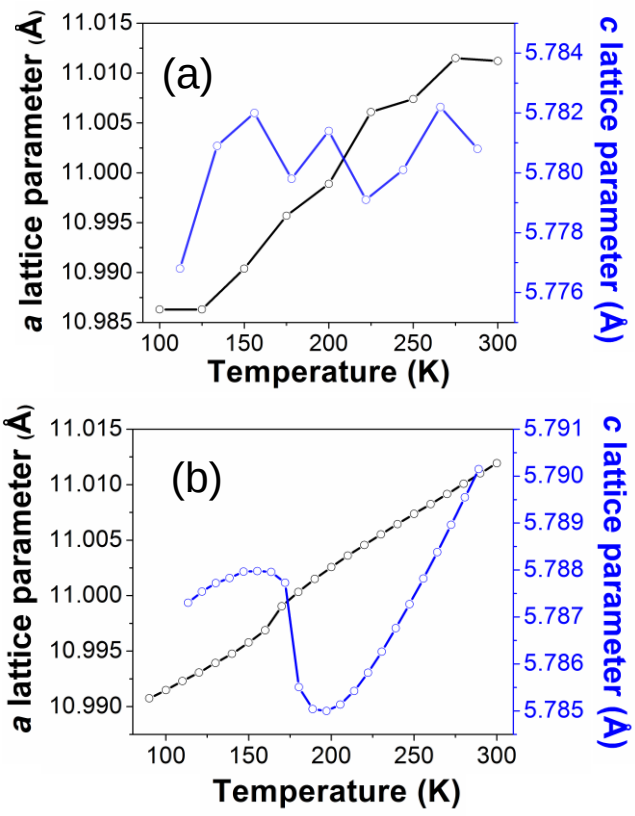

Figure 5. [*hk*0] planes measured in a single crystal of $Sm_2Ru_3Ge_5$ at (a) 164 K, (b) 174 K, and (c) 190 K. The data were collected using synchrotron X-ray diffraction on Sector 11-ID-D at the APS.

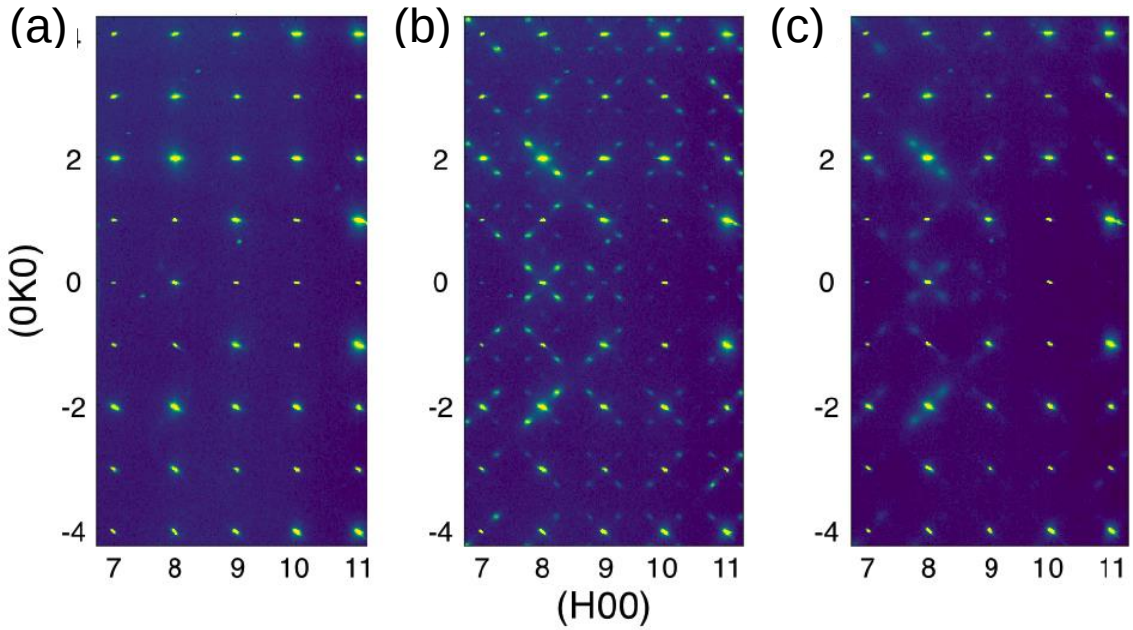

Figure 6. The intensity of the incommensurate peaks around [800] in $Sm_2Ru_3Ge_5$. The data were collected using synchrotron X-ray diffraction on Station A2 at CHESS.

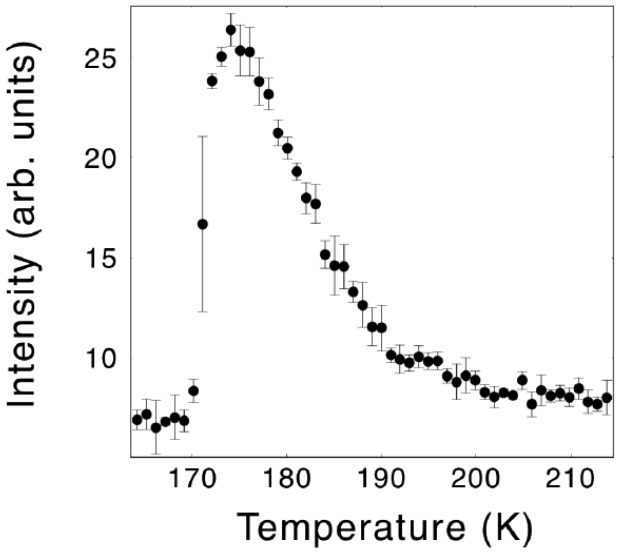

Figure 7. Ge11-Ge and Ge13-Ge distances along the modulation.

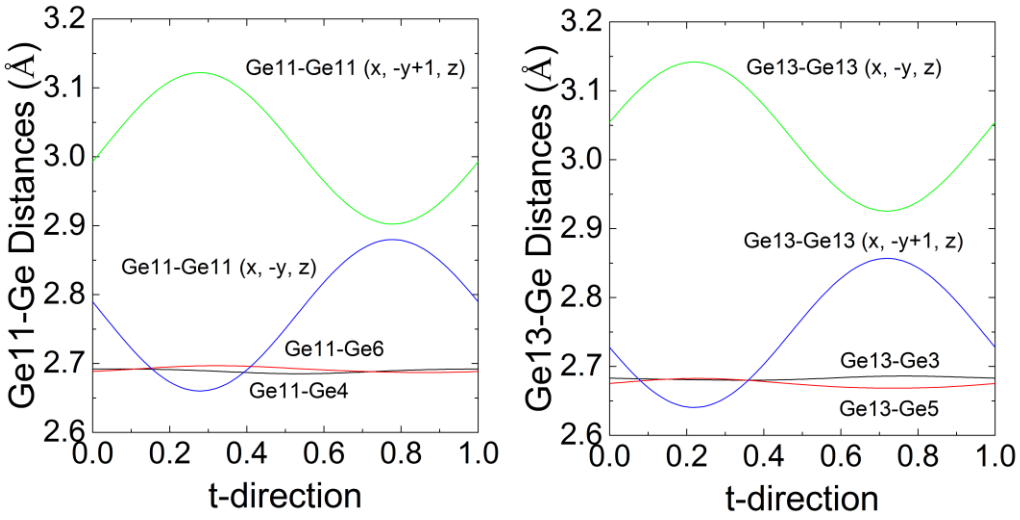

Figure 8. Electrical resistivity for $Sm_2Ru_3Ge_5$, as measured in the temperature range 1.8-350 K, upon both cooling and warming.

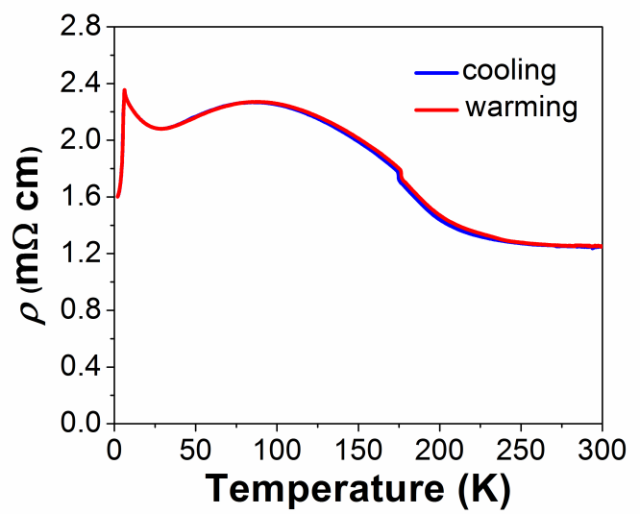

Figure 9. (a) The Hall coefficient (R_H) as a function of temperature for $Sm_2Ru_3Ge_5$. Inset: The magnetic field dependence of the Hall resistivity (ρ_{xy}) at various temperatures. (b) The electron concentration (n) as a function of temperature.

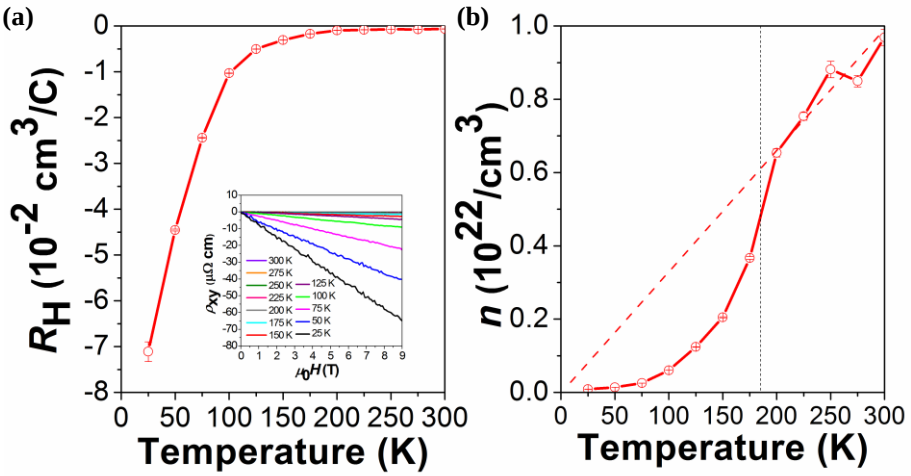

Figure 10. (a) Magnetic field dependence of magnetoresistance (MR) for $Sm_2Ru_3Ge_5$ at different temperatures. (b) MR under a field of 9 T at various temperatures.

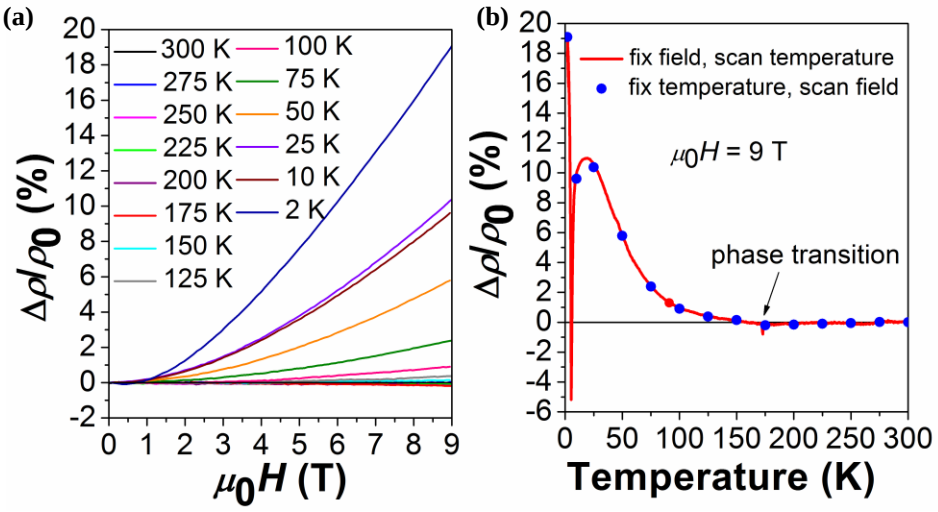

Figure 11. (a) Magnetic susceptibility, χ_m (black), for $Sm_2Ru_3Ge_5$, as measured at 1 kOe in the temperature range 1.8-350 K. Note the log scale for the temperature. Inset: Zero-field-cooled (ZFC) and field-cooled (FC) magnetic susceptibility as measured at 50 Oe in the temperature range 1.8-10 K. (b) Magnetization as a function of field as measured at 5 K. Inset: Enlarged view (between -5 and 5 kOe) of the magnetization as a function of field as measured at 5 K.

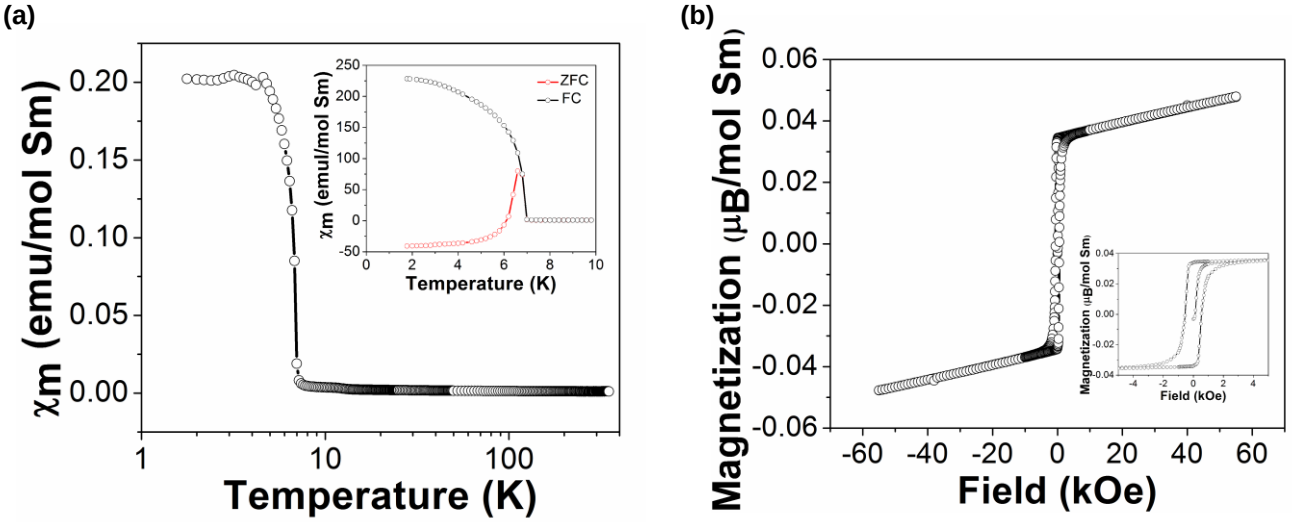

Figure 12. (a) Magnetic susceptibility, χ_m (black), and inverse magnetic susceptibility, $1/\chi_m$ (blue), for $Pr_2Ru_3Ge_5$, as measured at 1 kOe in the temperature range 1.8-350 K. (b) Derivative of $\chi_m T$ with respect to temperature. (c) Magnetization as a function of field as measured at 2 K and 300 K.

Figure 13. (a) Temperature dependence of the specific heat (C) for $Sm_2Ru_3Ge_5$ in the low-temperature region. (b) Plot of C/T versus T^2 showing the Debye fitting in the low-temperature region. (c) Temperature dependence of the specific heat for $Sm_2Ru_3Ge_5$ in the high-temperature region. (d) Temperature dependence of the specific heat for $Pr_2Ru_3Ge_5$ in the high-temperature region.

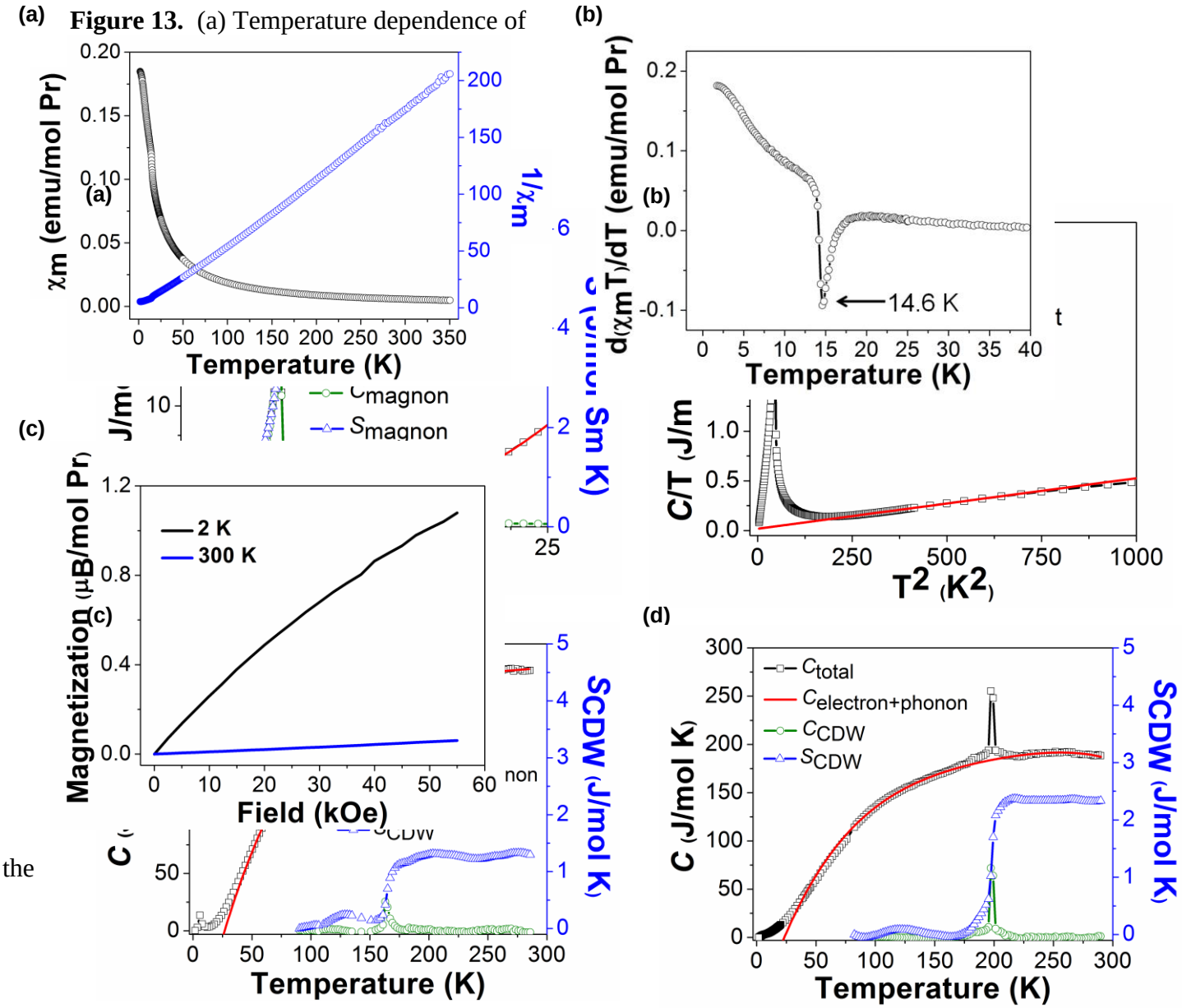

Figure 14. Sm L_{III} absorption edge spectra taken from a polycrystalline sample of $Sm_2Ru_3Ge_5$ at 20 K, 150 K, and 295 K.

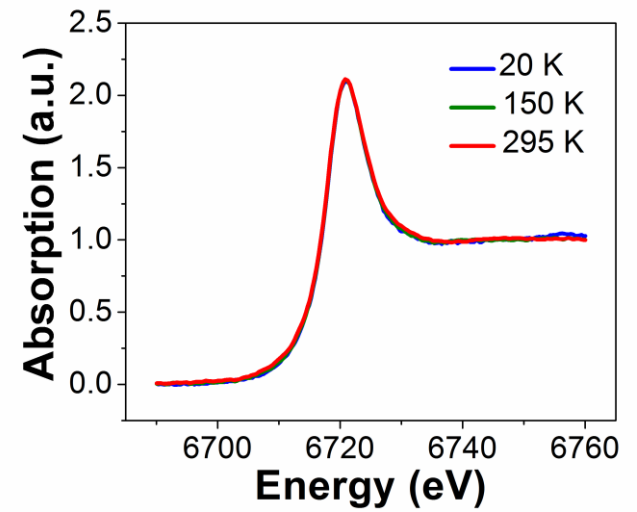

Figure 15. Projected density of states (PDOS) calculated by the GGA+U method for $Pr_2Ru_3Ge_5$, $Sm_2Ru_3Ge_5$, and $Dy_2Ru_3Ge_5$. The DOS are projected on the Ru *d*, Ge *p*, and rare-earth *d* and *f* orbitals. The calculated Fermi level is set equal to the zero of the energy.

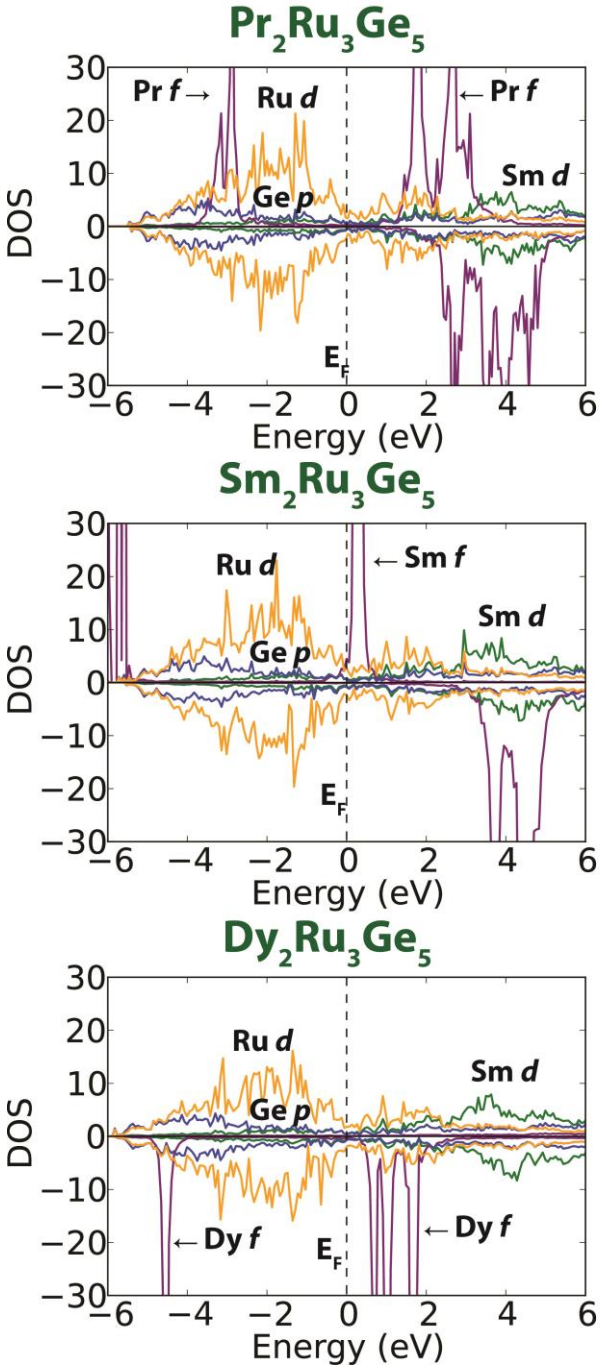

Figure 16. Electron energy bands calculated by the GGA+U method for $Pr_2Ru_3Ge_5$, $Sm_2Ru_3Ge_5$, and $Dy_2Ru_3Ge_5$. The calculated Fermi level is set equal to the zero of the energy. The upper and lower panels respectively show the band dispersion for the spin-up and spin-down eigenvalues calculated for the ferromagnetic solutions obtained by the self-consistent charge and magnetization density optimization.

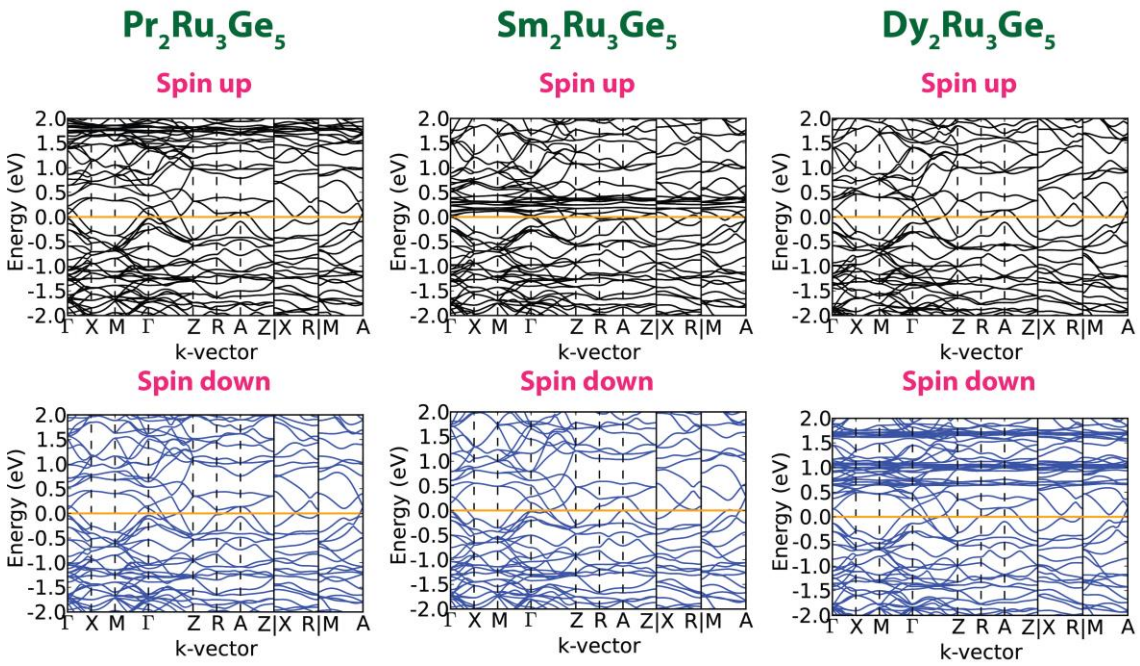

For Table of Contents Only

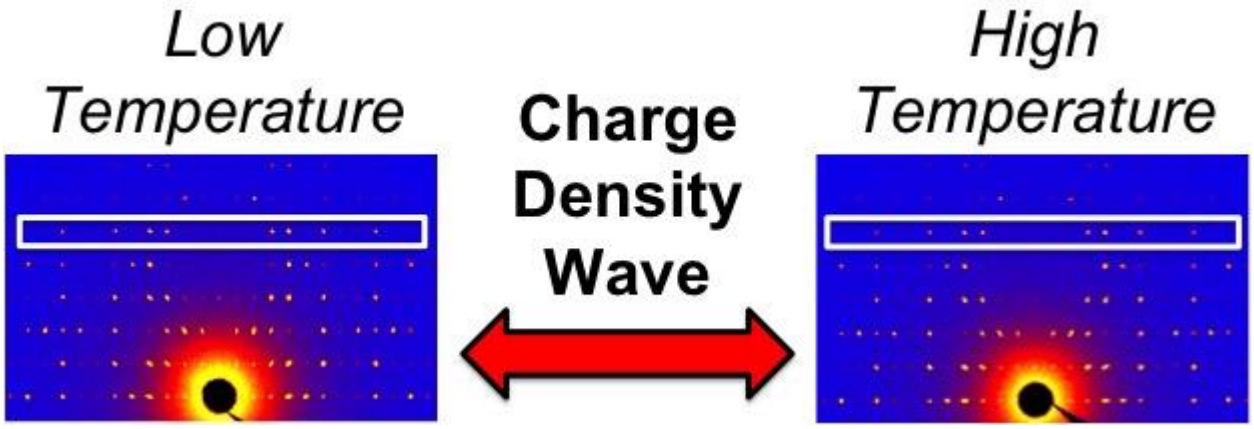

Novel Polymorphs of $RE_2Ru_3Ge_5$ (*RE* = Pr, Sm, Dy) Exhibiting Charge Density Wave Behavior

Daniel E. Bugaris,[†] Fei Han,[†] Christos D. Malliakas,[‡] Nicholas P. Calta,[‡] Mihai Sturza,[†,◊] Matthew Krogstad,[†,Δ] Raymond Osborn,[†] Stephan Rosenkranz,[†] Jacob P.C. Ruff,[∂] Giancarlo Trimarchi,[ǁ] Sergey L. Bud'ko,[§] Mahalingam Balasubramanian,[⊥] Duck Young Chung,[†] Mercouri G. Kanatzidis[*,†,‡]

[†] *Materials Science Division, Argonne National Laboratory, Argonne, IL 60439, USA*

[‡] *Department of Chemistry, Northwestern University, Evanston, IL 60208, USA*

[◊] *Leibniz Institute for Solid State and Materials Research Dresden IFW, Institute for Solid State Research, 01069 Dresden, Germany*

[Δ] *Department of Physics, Northern Illinois University, DeKalb, IL 60115, USA*

[∂] *Cornell High Energy Synchrotron Source, Cornell University, Ithaca, NY 14583, USA*

[ǁ] *Department of Physics and Astronomy, Northwestern University, Evanston, IL 60208, USA*

[§] *Division of Materials Science & Engineering, Ames Laboratory, and Department of Physics and Astronomy, Iowa State University, Ames, IA 50011, USA*

[⊥] *X-ray Science Division, Argonne National Laboratory, Argonne, IL 60439, USA*

SUPPORTING INFORMATION

Table S1. Atomic Coordinates and Equivalent Isotropic Displacement Parameters ($Å^2 \times 10^3$) for $Sm_2Ru_3Ge_5$ at 100 K

	x	*y*	*z*	U_{eq}[a]
Sm(1)	0.6809(1)	0	0.0520(1)	2(1)
Sm(2)	0.3483(1)	0.5	-0.2842(1)	3(1)
Sm(3)	0.1830(1)	0.5	0.0239(1)	3(1)
Sm(4)	1.3746(1)	0	0.2167(1)	2(1)
Sm(5)	0.8468(1)	0	-0.6432(1)	3(1)
Sm(6)	1.0427(1)	0.5	-0.4482(1)	2(1)
Sm(7)	0.8757(1)	0.5	-0.1441(1)	2(1)
Sm(8)	1.5406(1)	0	-0.4758(1)	3(1)
Ru(1)	0.7541(1)	0.5	0.1645(1)	3(1)
Ru(2)	1.2332(1)	0	-0.3551(1)	1(1)
Ru(3)	0.9686(1)	0	-0.3350(1)	2(1)
Ru(4)	1.2543(1)	0	-0.0892(1)	2(1)
Ru(5)	0.4873(1)	0.5	0.1440(1)	3(1)
Ru(6)	0.7332(1)	0.5	-0.5702(1)	1(1)
Ru(7)	0.9873(1)	0	-0.0693(1)	2(1)
Ru(8)	0.4684(1)	0.5	-0.5895(1)	1(1)
Ru(9)	1.1100(1)	0.2505(1)	0.2880(1)	1(1)
Ru(10)	0.6095(1)	0.2506(1)	-0.2133(1)	2(1)
Ge(1)	0.6412(2)	0.5	-0.0325(2)	2(1)
Ge(2)	1.4300(2)	0	-0.2419(2)	2(1)
Ge(3)	1.1404(2)	0	0.1060(2)	2(1)
Ge(4)	0.2920(2)	0.5	0.2572(2)	1(1)
Ge(5)	0.9303(2)	0.5	-0.6832(2)	3(1)
Ge(6)	1.0807(2)	0	-0.5320(2)	2(1)
Ge(7)	1.1100(2)	0.2520(2)	-0.2113(2)	2(1)
Ge(8)	0.5813(2)	0.5	-0.3941(2)	2(1)
Ge(9)	0.7918(2)	0	-0.1823(2)	2(1)
Ge(10)	0.6109(2)	0.2492(2)	0.2882(2)	2(1)
Ge(11)	1.2904(1)	0.2395(2)	-0.5402(2)	3(1)
Ge(12)	0.7863(1)	0.2508(2)	-0.3862(2)	7(1)
Ge(13)	0.9392(1)	0.2623(2)	0.1084(2)	5(1)
Ge(14)	0.4348(1)	0.2496(2)	-0.0350(2)	5(1)

[a] U_{eq} is defined as one third of the trace of the orthogonalized U_{ij} tensor.

Table S2. Anisotropic Displacement Parameters ($Å^2 \times 10^3$) for $Sm_2Ru_3Ge_5$ at 100 K [a]

	U_{11}	U_{22}	U_{33}	U_{12}	U_{13}	U_{23}
Sm(1)	1(1)	2(1)	2(1)	0	0(1)	0
Sm(2)	2(1)	4(1)	3(1)	0	-2(1)	0
Sm(3)	4(1)	2(1)	3(1)	0	-2(1)	0
Sm(4)	1(1)	4(1)	3(1)	0	1(1)	0
Sm(5)	2(1)	1(1)	5(1)	0	-1(1)	0
Sm(6)	4(1)	2(1)	1(1)	0	1(1)	0
Sm(7)	2(1)	1(1)	4(1)	0	2(1)	0
Sm(8)	5(1)	3(1)	1(1)	0	0(1)	0
Ru(1)	1(1)	5(1)	2(1)	0	-3(1)	0
Ru(2)	1(1)	2(1)	2(1)	0	1(1)	0
Ru(3)	2(1)	2(1)	2(1)	0	0(1)	0
Ru(4)	2(1)	4(1)	1(1)	0	0(1)	0
Ru(5)	1(1)	5(1)	3(1)	0	-5(1)	0
Ru(6)	1(1)	2(1)	1(1)	0	4(1)	0
Ru(7)	1(1)	4(1)	1(1)	0	-2(1)	0
Ru(8)	2(1)	1(1)	1(1)	0	3(1)	0
Ru(9)	1(1)	1(1)	2(1)	-2(1)	0(1)	-1(1)
Ru(10)	2(1)	1(1)	2(1)	0(1)	0(1)	-2(1)
Ge(1)	2(1)	3(1)	2(1)	0	-1(1)	0
Ge(2)	2(1)	2(1)	2(1)	0	0(1)	0
Ge(3)	2(1)	4(1)	1(1)	0	-1(1)	0
Ge(4)	1(1)	1(1)	2(1)	0	0(1)	0
Ge(5)	4(1)	4(1)	2(1)	0	0(1)	0
Ge(6)	2(1)	1(1)	2(1)	0	-1(1)	0
Ge(7)	2(1)	2(1)	2(1)	0(1)	0(1)	1(1)
Ge(8)	2(1)	1(1)	3(1)	0	2(1)	0
Ge(9)	2(1)	1(1)	1(1)	0	0(1)	0
Ge(10)	2(1)	2(1)	2(1)	1(1)	0(1)	-2(1)
Ge(11)	2(1)	5(1)	3(1)	-1(1)	-2(1)	2(1)
Ge(12)	6(1)	7(1)	8(1)	6(1)	1(1)	6(1)
Ge(13)	6(1)	6(1)	3(1)	3(1)	1(1)	-3(1)
Ge(14)	6(1)	2(1)	6(1)	-5(1)	4(1)	-5(1)

[a] The anisotropic displacement factor exponent takes the form: $-2\pi^2[h^2a^{*2}U_{11} + ... + 2hka^*b^*U_{12}]$.

Table S3. Fourier components of the displacive modulation *q* vector for $Sm_2Ru_3Ge_5$ at 100 K

	axis	cos displacement	sin displacement
Sm(1)	x	-0.00039(18)	0.0005
Sm(1)	y	0	0
Sm(1)	z	0.00031(13)	0.00026(13)
Sm(2)	x	0.00000(13)	0.00026(11)
Sm(2)	y	0	0
Sm(2)	z	0.00096(16)	0.0004(3)
Sm(3)	x	-0.00112(15)	0.0004(3)
Sm(3)	y	0	0
Sm(3)	z	0.0004(2)	0.00056(16)
Sm(4)	x	0.00001(12)	0.00024(11)
Sm(4)	y	0	0
Sm(4)	z	0.00152(18)	-0.0005(4)
Sm(5)	x	-0.00017(11)	0.00014(12)
Sm(5)	y	0	0
Sm(5)	z	0.00169(12)	0.0001(5)
Sm(6)	x	-0.0012(3)	0.0009(3)
Sm(6)	y	0	0
Sm(6)	z	0.00035(13)	0.00023(16)
Sm(7)	x	-0.00017(13)	0.00022(12)
Sm(7)	y	0	0
Sm(7)	z	0.00081(12)	-0.0001(2)
Sm(8)	x	-0.00086(11)	0.0003(3)
Sm(8)	y	0	0
Sm(8)	z	0.00040(15)	0.00031(15)
Ru(1)	x	0.00053(17)	0.0001(2)
Ru(1)	y	0	0
Ru(1)	z	-0.0003(2)	0.0004(2)
Ru(2)	x	0.00046(16)	0.0001(2)
Ru(2)	y	0	0
Ru(2)	z	-0.0005(2)	0.0004(2)
Ru(3)	x	-0.00004(19)	0.00035(16)
Ru(3)	y	0	0

Ru(3)	z	-0.0003(3)	0.0007(2)
Ru(4)	x	0.00000(19)	0.00032(16)
Ru(4)	y	0	0
Ru(4)	z	-0.00036(18)	0.0001(2)
Ru(5)	x	0.00041(17)	-0.00018(19)
Ru(5)	y	0	0
Ru(5)	z	0.0002(2)	0.00033(19)
Ru(6)	x	0.00042(18)	0.00032(19)
Ru(6)	y	0	0
Ru(6)	z	0.00027(19)	0.00027(19)
Ru(7)	x	0.00033(16)	-0.00010(18)
Ru(7)	y	0	0
Ru(7)	z	-0.0005(2)	0.0007(2)
Ru(8)	x	0.00062(17)	0.0002(2)
Ru(8)	y	0	0
Ru(8)	z	-0.00057(19)	0.0003(2)
Ru(9)	x	0.00034(10)	0.00005(16)
Ru(9)	y	-0.0002(3)	-0.00035(14)
Ru(9)	z	-0.00039(13)	0.0004(2)
Ru(10)	x	-0.00005(10)	0.00010(13)
Ru(10)	y	-0.0002(3)	-0.00024(15)
Ru(10)	z	0.00021(9)	0.00013(18)
Ge(1)	x	-0.0002(2)	0.0002(2)
Ge(1)	y	0	0
Ge(1)	z	0.0003(2)	-0.0001(3)
Ge(2)	x	-0.0001(1)	0.0001(2)
Ge(2)	y	0	0
Ge(2)	z	0.0004(3)	0.0003(3)
Ge(3)	x	0.0006(2)	0.0001(3)
Ge(3)	y	0	0
Ge(3)	z	-0.0006(2)	0.0002(3)
Ge(4)	x	0.0002(2)	0.0000(2)
Ge(4)	y	0	0
Ge(4)	z	-0.0005(3)	0.0004(3)
Ge(5)	x	0.0007(2)	0.0002(3)

Ge(5)	y	0	0
Ge(5)	z	-0.0005(3)	0.0004(3)
Ge(6)	x	0.0005(2)	-0.0002(2)
Ge(6)	y	0	0
Ge(6)	z	-0.0001(2)	0.0003(2)
Ge(7)	x	-0.00012(14)	0.00025(19)
Ge(7)	y	-0.0002(3)	0.00011(18)
Ge(7)	z	0.0000(2)	0.0006(2)
Ge(8)	x	0.0000(2)	0.0003(2)
Ge(8)	y	0	0
Ge(8)	z	0.0000(2)	0.0001(2)
Ge(9)	x	-0.0001(2)	0.0000(2)
Ge(9)	y	0	0
Ge(9)	z	0.0003(2)	0.0003(2)
Ge(10)	x	0.00011(14)	0.00025(19)
Ge(10)	y	-0.0001(3)	0.00012(17)
Ge(10)	z	0.00043(11)	0.0000(3)
Ge(11)	x	-0.0027(3)	0.0009(7)
Ge(11)	y	0.0089(9)	-0.003(2)
Ge(11)	z	0.0027(2)	-0.0005(7)
Ge(12)	x	-0.00049(19)	0.0003(2)
Ge(12)	y	-0.0019(3)	0.0003(6)
Ge(12)	z	0.0003(2)	0.0002(2)
Ge(13)	x	-0.0029(3)	0.0009(8)
Ge(13)	y	-0.0089(8)	0.003(2)
Ge(13)	z	0.0030(2)	-0.0005(8)
Ge(14)	x	-0.00002(17)	0.0010(17)
Ge(14)	y	-0.0016(4)	0.0007(5)
Ge(14)	z	0.0006(2)	0.0001(2)